Model of Spectral and Directional Radiative Transfer in Complex Urban Canopies with Participating Atmospheres

Cyril Caliot, Robert Schoetter, Vincent Forest, Vincent Eymet, Tin-Yuet Chung

Noname manuscript No.
(will be inserted by the editor)

Model of Spectral and Directional Radiative Transfer in Complex Urban Canopies with Participating Atmospheres

Cyril Caliot · Robert Schoetter · Vincent Forest · Vincent Eymet · Tin-Yuet Chung

Submitted version 2022 in journal Boundary-Layer Meteorology (Springer Nature):
http://www.doi.org/10.1007/s10546-022-00750-5

Abstract
Thermal heat transfers, including solar and infrared radiation in cities, are key processes for studying urban heat islands, outdoor human thermal comfort, energy consumption, and production. Thus, accurate radiative transfer models are required to compute the solar and infrared fluxes in complex urban geometry accounting for the spectral and directional properties of the atmosphere and city fabric materials. In addition, these reference models may be used to evaluate existing parametrization models of radiative heat transfer and to develop new ones. The present article introduces a new reference model for outdoor radiative exchange based on the backward Monte Carlo method. The integral formulations of the direct and scattered solar, and the terrestrial infrared radiative flux densities are presented. This model can take into account the ground (e.g., roads, grass), different types of buildings and vegetation (e.g., trees consisting of opaque leaves and trunks) with their spectral and directional (Lambertian and specular) reflectivity of materials. Numerical validations of the algorithm are presented against the results of a state-of-the-art model based on the radiosity method for the particular case of an infinitely long street canyon. In addition, the convergence of urban solar radiation budgets is studied for a selection of urban complex geometries including

C. Caliot
CNRS, UPPA, E2S, LMAP, 1 Allée du Parc Montaury, Anglet, France
Tel.: +335-59-574266
E-mail: cyril.caliot@cnrs.fr

R. Schoetter
CNRM, Université de Toulouse, Météo-France, CNRS, 42 avenue Gaspard Coriolis, Toulouse, France

V. Forest
Meso-Star SAS, Longages, France

V. Eymet
Meso-Star SAS, Longages, France

T.-Y. Chung
CNRM, Université de Toulouse, Météo-France, CNRS, 42 avenue Gaspard Coriolis, Toulouse, France

or not the window glazing. Good convergence is found for all geometries, even in the presence of rare events due to specular reflections.

Keywords Reference Monte Carlo method · Solar radiation · Thermal infrared radiation · Three-dimensional radiative transfer · Urban form

1 Introduction

Cities exhibit a specific local climate, since the urban surface–atmosphere momentum and energy exchange differs from rural areas (Oke 1982). Obstacles like buildings and trees make cities aerodynamically rough compared to open rural environments, leading to reduced average near-surface wind speed but potentially higher turbulence intensity (Moonen et al. 2012). As a consequence, pedestrian wind comfort might be deteriorated and wind stress on infrastructure enhanced. Due to the prevalence of impervious surfaces, evapotranspiration by vegetation is reduced in cities, causing higher sensible and lower latent heat fluxes. The three-dimensional city geometry and construction materials with high heat capacity lead to heat storage at daytime and release at night-time, which is one of the main causes of the urban heat island effect (UHI) (Arnfield 2003). The three-dimensional city geometry with a variety of building types, vegetation elements, or other obstacles with different shape, size, orientation, and reflectivity (albedo) also affects the solar and infrared radiative exchange. Shading and multiple reflections of solar radiation (Krayenhoff et al. 2014) by buildings or vegetation cause a strong modification of solar radiation received by different facets compared to an open environment. Multiple reflections of solar radiation lead to a lower aggregated city albedo compared to a flat surface with the same albedo of individual facets. The terrestrial infrared radiation is subject to multiple reflections, absorption, and emission (radiative trapping). As a consequence, at night, net longwave radiation exchange with the sky may be increased if the materials are isothermal, but this exchange depends on the spatial distribution of materials having different temperatures (Krayenhoff et al. 2014). Both the reduction of aggregated city albedo and the infrared radiation trapping contribute to the UHI.

With increasing urbanization (UN 2019) and projected global climate change (Collins et al. 2013), the combination of increasing regional air temperature, more frequent heat waves, and a potentially stronger UHIs due to larger cities lead to high risk for humans and infrastructure in future cities. Urban radiative exchange is a crucial process for urban planning as well as climate change mitigation and adaptation since it affects the local meteorological conditions (UHI) and is also a key factor in the control of outdoor human thermal comfort (Ali-Toudert and Mayer 2006, 2007a,b) and building energy consumption (Strømann-Andersen and Sattrup 2011; Frayssinet et al. 2018), which is responsible for 40% of the worldwide primary energy consumption (Yang et al. 2014). The street geometry and orientation regulates the solar access. For example, at mid- and high latitudes, in a city with a low aspect ratio of street canyons (building height divided by typical street width), more solar radiation will reach the ground and facades during the winter season than in a city with a high aspect ratio (Ko 2013). The albedo of different urban facets can be modified to improve inhabitants' comfort or reduce building energy consumption (e.g., high albedo in warm climates, Akbari

et al. 2001). Windows, which reflect specularly solar radiation, are often a major component of the shell of buildings. Solar panels might be installed on the roofs of buildings (Masson et al. 2014) and the specular and angular properties of the incoming solar radiation need to be known precisely to predict the photovoltaic electricity production (Lindsay et al. 2020). Numerical models with an accurate representation of the radiative exchange in a complex urban geometry are thus required for the assessment of the effect of climate change mitigation and adaptation measures implemented in cities. Such models can operate at two scales. At the obstacle-resolving scale (microscale, about 1 m resolution), the complex three-dimensional building geometry is simulated explicitly whereas mesoscale (100 m to 10 km horizontal resolution) and global models treat the urban land surface as flat, and urban land surface models (Grimmond et al. 2010, 2011) can be employed to parametrize the effect of three-dimensional geometry by calculating the urban surface energy balance assuming a strongly simplified urban geometry (e.g., an infinitely long street canyon). Obstacle-resolving models might be employed to serve as a reference to quantify the uncertainties due to the simplification of physical processes and urban geometry in the urban land surface models.

The present article introduces a new reference model for outdoor urban radiative transfer, which is based on the Monte Carlo method (MCM). This method is well established for solving the radiative transfer equation (RTE) in a medium which potentially emits, absorbs, and scatters radiation (Farmer and Howell 1998; Howell 1998; Modest 2003; Delatorre et al. 2014). Thanks to null-collision algorithms (Galtier et al. 2013) for heterogeneous media and ray-tracing accelerating grids (Villefranque et al. 2019), MCM algorithms deliver reference results with a computation time insensitive to the atmospheric composition (gases, clouds, aerosols, etc.). The introduced urban MCM model builds on the previous work of Villefranque et al. (2019), which deals with radiative transfer in a cloudy atmosphere. Their work is extended here to deal with urban geometries and to calculate the radiative flux density in the urban environment. The new reference model has two main purposes: 1) To quantify radiative observables like the solar and infrared radiation incident on buildings, urban vegetation, and humans by taking into account the complex urban geometry, the spectral, and directional reflectivities of urban materials. This reference model can be used for urban planning and design at the building and vegetation-resolving scale; 2) to quantify the uncertainties of simplifications of the urban geometry and radiative exchange processes made in mesoscale urban land surface models, which can help to guide potential future developments of these models.

The objectives of the present article are: 1) to give a brief overview of the state of the art in urban radiative transfer modelling at the microscale (Sect. 2); 2) to present the integral formulation of the radiative heat transfer model solved with MCM in complex urban geometry (Sect. 3) and the employed data (Sect. 4); 3) to validate the reference MCM model to a state-of-the-art radiosity model in a street-canyon geometry as well as the closure of the simulated urban radiation budget (Sect. 5). Conclusions and outlook are given in Sect. 6.

2 Obstacle-Resolving Radiative Transfer Modelling in Urban Areas

There exist three main methods for the modelling of three-dimensional radiative exchange in urban areas at the obstacle-resolving scale. These are the radiosity method, the discrete ordinates method (DOM), and the MCM. These three methods have very specific strengths and weaknesses which shall be briefly explained.

The standard radiosity method is based on a discretisation of the urban facets and the sky vault into N_f small opaque and Lambertian elements (facets) where spatially uniform radiosities are assumed. Furthermore, the medium is considered transparent, which means there is no scattering, emission, or absorption by air in between the facets. A matrix of so-called view factors is computed, which stores the information about the fraction of radiation leaving facet i ($1 \leq i \leq N_f$) that will be intercepted by facet j ($1 \leq j \leq N_f$). When incoming radiation from the sky vault, the reflectivity, and the temperature of all facets are known, the radiative fluxes incident on each facet can be calculated by solving a linear system of N_f coupled equations in matrix form. Under the assumption that the urban geometry does not change during the simulation, the computationally expensive view factor calculation can be done once during the model initialisation. During the simulation, the numerical cost depends on the number of facets and the complexity of the system to solve. The radiosity method is commonly used in daylight simulation tools and micrometeorological models like ENVI-met (Bruse and Fleer 1998), SOLENE (Vinet 2000; Miguet and Groleau 2002; Musy et al. 2015), LASER/F (Roupioz et al. 2018), and PALM-4U (Resler et al. 2017; Krč et al. 2021). A major disadvantage of the radiosity method is that large matrices of view factors have to be stored in memory (Milliez 2006), especially for large model domains with many facets, and when considering specular reflections (Aguerre et al. 2019). Krč et al. (2021) present a method to reduce the number of view factors by excluding those facets which contribute only little to the irradiance or are too far from a specific facet. Furthermore, they propose to regroup facets that are close to each other, assuming that radiative properties are smooth in space. Such simplifications will slightly reduce the accuracy of the results. Radiation models based on the radiosity method split radiation into the solar and thermal infrared part (Morille et al. 2015; Resler et al. 2017). Taking into account many spectral intervals increases computational time. Urban vegetation cannot be explicitly simulated, since the representation of individual leaves would lead to a prohibitively high number of facets. It can therefore only be represented as an attenuation factor proportional to the leave area density in the view factors between the facets (Krč et al. 2021). The DOM is based on solving the three-dimensional RTE in participating media with a numerical grid and for a finite number of directions (ordinates). DOM can deal with non-isothermal, heterogeneous, non-grey media, anisotropic scattering, and reflection in three-dimensional complex geometry. Thus, scattering, emission, and absorption of radiation by the medium (gases, clouds, and aerosols) can be considered, unlike the radiosity method, which is beneficial in situations with fog or smoke between the buildings (Qu et al. 2011) or with high humidity or rainfall (Resler et al. 2017). The accuracy of three-dimensional radiative transfer solved by DOM is limited by ray effects and false scattering originating from angular and spatial discretization, respectively. Several proposals have been made to reduce these limitations (Coelho 2002). Increasing the number of directions and a finer spatial discretization are two possible solutions that increase the

computational cost and limit the use of DOM to cases where the computational burden is acceptable. A widely-used radiation model based on DOM is the Discrete Anisotropic Radiative Transfer (DART) model (Gastellu-Etchegorry 2008; Gastellu-Etchegorry et al. 2015), which can solve radiative transfer in any spectral band from ultraviolet to the thermal infrared and consider the presence of opaque obstacles (roads, walls, roofs, and vegetation). DART has been applied to urban areas in various ways. Landier et al. (2018) used DART in combination with satellite observations to calculate the aggregated albedo and shortwave radiation budget of urban canopies. They compared DART results with flux tower observations and showed that DART captures well the urban radiation budget. In a similar application, Dissegna et al. (2019) used DART to analyze the radiation budget of a city and its sensitivity to changing vegetation characteristics. Morrison et al. (2018, 2020, 2021) used DART in combination with observations of broadband longwave radiation fluxes by a network of ground-based cameras to derive the urban surface temperature at high spatial resolution. Stretton et al. (2022) use the DART model as a reference to evaluate the mesoscale urban radiation scheme SPARTACUS-Urban (Hogan 2019a,b). DOM was also used by Milliez (2006) to calculate radiative exchanges in a micrometeorological model with the DOM-based SYRTHES code (Rupp and Péniguel 2014) coupled to the computational fluid dynamics Code_Saturne. This coupled model has been validated for the Mock Urban Setting Test (MUST) experiment (Milliez 2006; Qu et al. 2011) and good model performance has been found.

Unlike previous deterministic methods (radiosity and DOM), MCM is a stochastic meshless method requiring only the geometry associated to each material and allowing the simulation of three-dimensional complex geometry with high scale ratio. In three-dimensional radiative heat transfer, MCM is used to solve for linear integrals of the radiative intensity which is formulated as the integral solution of the RTE. The main advantage of MCM is to be quasi independent of the integration domain size. This unique feature allows one to solve problems in heterogeneous and non-isothermal media with anisotropic scattering, reflection, and emission without additional computational burden. Thus, MCM results can include many complexities of the radiative heat transfer and they are often considered as reference results when comparing or validating approximate models. Each MCM sampling involves a realization of mixed random paths with multiple scattering and reflections that are pictured to be travelled by fictitious bundles of rays in forward or backward directions in the scene to deposit (Farmer and Howell 1998; Howell 1998; Modest 2003) or collect (Delatorre et al. 2014; Howell et al. 2020), respectively, the contributions from sources. The stochastic MCM estimation of an observable requires sampling and tracking of a large number of random paths to increase the confidence in the MCM estimate and decrease its associated standard error. As far as a single radiative observable is concerned (e.g., the solar irradiation on a specific surface), MCM may be considered more attractive than the DOM or radiosity method with the possibility to include more geometry details (e.g., tree leaves) and directional and spectral dependency at a lower computational cost. Indeed, mesh-based DOM and radiosity method need to compute and store in memory the entire radiation field to calculate this observable while MCM does not. However, if the field of a radiative observable (e.g., the solar irradiation on all surface elements of the orography) is searched in a specific mesh, the computational cost of DOM or radiosity method does not change whereas the cost for MCM increases

proportionally to the number of mesh elements. Nevertheless, even in this kind of calculation, MCM may still be attractive if the media's radiative properties (scattering phase function, reflectivity, emissivity) exhibit high spectral or directional dependency that prevent to use deterministic methods. It is therefore a reference method to calculate radiation, which, if carefully validated can be used to quantify the uncertainties of the other methods. Thomas et al. (2011) introduced a MCM model that is able to simulate the images seen by airborne or satellite sensors taking into account atmospheric aerosols and a three-dimensional urban scene with bidirectional reflection functions of materials. This MCM model has however not been used for the calculation of radiative flux densities in urban areas as it is made in the present study.

3 Modelling Radiative Transfer in a Cloudy Atmosphere in the Presence of Buildings and Vegetation

We present a model for the computation of solar and terrestrial infrared radiative flux densities. The model solves the integral form of the RTE solution with a MCM in a participating medium (Earth's atmosphere) involving non-grey absorption, emission, and anisotropic scattering. It is assumed that all radiative properties and temperature distributions are known for both the atmosphere and its boundaries, which are the top of atmosphere (TOA) and the Earth's surface made of vegetation and buildings. The atmosphere is described with the spatial distribution of the spectral and directional radiative properties of gases, liquid droplets, and solid particles. These properties are supplied by the user as data of absorption and scattering coefficients as well as scattering phase functions. A backward MCM algorithm with the technique of null-collision is used to tackle the nonlinearity of Beer's extinction law and enables the use of accelerating grids that improve the radiative properties availability during computation. Indeed, sampling a collision length (such as scattering, absorption, or extinction lengths) in heterogeneous media is difficult since the evolution of the optical thickness along the bundle of rays path is not known a priori. Null-collisions may be seen as an acceptance-rejection sampling technique (Galtier et al. 2013; El Hafi et al. 2021) which considers a constant value of the collision coefficient inside a volume where the bundle of rays travels. It accelerates the computation of collisions while the rejections (null-collisions) help recover the true optical thickness. The use of accelerating grids is described in Villefranque et al. (2019) and implemented in the publicly available htrdr code of Meso-Star (2021). Starting from htrdr, we developed a new code, htrdr-urban, based on the model presented in this section, that is enriched to compute radiative fluxes in three-dimensional complex geometry including the diversity of radiative properties of the materials that constitute the city fabric and the vegetation. Material surfaces are assumed opaque, Lambertian, or specular, with spectral dependency of their reflectivity. An important restriction of the model is that only the radiation reflected by the outer building envelope is tracked, while the unreflected radiation is assumed to be absorbed. Radiation that might be transmitted into the buildings (especially by windows), its propagation inside the building, and potential re-transmission from indoor to outdoor is not considered.

In the following, the expressions of incident flux density are derived for the direct (Sect. 3.1.1) and scattered (Sect. 3.1.2) solar radiation, and for the terrestrial infrared radiation (Sect. 3.2).

3.1 Solar Radiative Flux Density

The general expression of the instantaneous local total irradiation on a surface (radiative flux density) $\dot{q}$ (W m^{-2}) at position $\mathbf{x}_0$ is given by

$$\dot{q}(\mathbf{x}_0, t) = \int_0^{\infty} d\lambda \int_{2\pi} I(\mathbf{x}_0, t, -\boldsymbol{\omega}_0, \lambda)\ |\mathbf{n}(\mathbf{x}_0) \cdot \boldsymbol{\omega}_0|\ d\Omega(\boldsymbol{\omega}_0), \tag{1}$$

where t is the time (this dependency will be dropped for conciseness in the remainder of the text), λ the radiation wavelength, $\mathbf{n}$ the surface normal, $d\Omega$ the elementary solid angle around direction $\boldsymbol{\omega}_0$ (Fig. 1), and I the incident spectral radiative intensity. This integral is solved with a MCM algorithm, such as in Delatorre et al. (2014), that accounts for multiple reflections, spectral and directional optical properties to obtain a MCM estimate of the flux density $\tilde{q}$ associated with a standard error value $\tilde{\sigma}_{\tilde{q}}$ that helps to evaluate MCM convergence (see Sect. 6). To compute $\dot{q}$ (Eq. 1), the integrated form of the steady-state RTE needs to be solved inside the domain $\mathcal{D}$ (having a unit refractive index) with its boundary conditions on $\partial\mathcal{D}_{\mathcal{S}}$:

$$\begin{aligned}
&I(\mathbf{x}_j, -\boldsymbol{\omega}_j, \lambda) = \\
&\int_0^{+\infty} d\ell_{j+1}\ \underbrace{\exp\left[-\int_0^{\ell_{j+1}} \beta(\mathbf{x}, \lambda)\, d\ell\right]}_{\text{transmission}} \Bigg(\\
&\underbrace{\mathcal{H}(\mathbf{x}_{j+1} \in \mathcal{D})}_{\text{test function}} \Bigg[\underbrace{\kappa(\mathbf{x}_{j+1}, \lambda) I_b(\mathbf{x}_{j+1}, \lambda)}_{\text{volume emission}} + \\
&\underbrace{\sigma_s(\mathbf{x}_{j+1}, \lambda) \int_{4\pi} p(\mathbf{x}_{j+1}, \boldsymbol{\omega}_j | \boldsymbol{\omega}_{j+1}, \lambda)\, d\Omega'(\boldsymbol{\omega}_{j+1})\, I(\mathbf{x}_{j+1}, -\boldsymbol{\omega}_{j+1}, \lambda)}_{\text{in-scattering}} \Bigg] + \\
&\mathcal{H}(\mathbf{x}_{j+1} \in \partial\mathcal{D}_{\mathcal{S}}) \Bigg[\underbrace{\varepsilon'(\mathbf{x}_{j+1}, \boldsymbol{\omega}_j, \lambda)\, I_b(\mathbf{x}_{j+1}, \lambda)}_{\text{surface emission}} + \\
&\underbrace{\int_{2\pi} f_r(\mathbf{x}_{j+1}, \boldsymbol{\omega}_j | \omega', \lambda)\, I(\mathbf{x}_{j+1}, -\boldsymbol{\omega}_{j+1}, \lambda)\, |\mathbf{n}(\mathbf{x}_{j+1}) \cdot \boldsymbol{\omega}_{j+1}|\ d\Omega'(\boldsymbol{\omega}_{j+1})}_{\text{reflection}} \Bigg] + \\
&\mathcal{H}(\mathbf{x}_{j+1} \in \partial\mathcal{D}_d) \quad \underbrace{I_{d,ex}}_{\text{Sun's emission}} \Bigg).
\end{aligned} \tag{2}$$

At position $\mathbf{x}_{j+1} = \mathbf{x}_j + \boldsymbol{\omega}_j \ell_{j+1}$ (Fig. 1), a radiative event occurs (absorption, emission, scattering, or reflection) involving other unknown radiative intensities. A radiative path is built from these positions separated by a distance $\ell_{j+1} = \|\mathbf{x}_j - \mathbf{x}_{j+1}\|$ with the subscript index j that is increasing with the number of events counted in the reverse direction (from the path end, $\mathbf{x}_0$, to the source).

Indeed, to highlight the backward MCM algorithm, the path directions, $\boldsymbol{\omega}_j$, are considered reversed compared to the forward physical path directions, which are directed from the Sun to $\mathbf{x}_j$ (see Fig. 1). The extinction coefficient $\beta(\mathbf{x},\lambda) = \kappa(\mathbf{x},\lambda)+\sigma_s(\mathbf{x},\lambda)$ is the sum of absorption and scattering coefficients, respectively; I_b is the Planck's law of the Blackbody; p is the scattering phase function expressed as a probability density function (PDF); ε' is the directional emissivity of the surface and f_r its bidirectional reflectivity distribution function (BRDF). The expression of I in Eq. 2 includes the radiative intensity sources inside the domain $\mathcal{D}$ (volumetric emission and in-domain scattering), and at its boundary $\partial\mathcal{D}_\mathcal{S}$ (opaque surface emission and reflection) comprising Lambertian ($\partial\mathcal{D}_{\mathcal{S}_L}$) and specular ($\partial\mathcal{D}_{\mathcal{S}_F}$) surfaces. To gather the formulation of domain and boundary sources in one expression (Eq. 2), a test function $\mathcal{H}(\cdot)$ is used taking a unity value if its condition is fulfilled and zero otherwise. At TOA ($\partial\mathcal{D}_{TOA}$), the value of downwelling I is the extraterrestrial solar radiative intensity $I_{d,ex}$ inside the solar cone $\Delta\Omega_d$. To compute specifically the solar total radiative flux density, best convergence can be achieved by splitting the radiative intensity between a direct solar contribution I_d and a (multi-)scattered component I_{sc}: $I = I_d + I_{sc}$. Introducing this splitting into Eq. 1 leads to $\dot{q}(\mathbf{x}_0) = \dot{q}_d(\mathbf{x}_0)+\dot{q}_{sc}(\mathbf{x}_0)$. In the next two sections, the integral formulations of these solar fluxes are presented.

3.1.1 Direct Solar Flux Density

To compute $\dot{q}_d(\mathbf{x}_0)$, which is the direct solar flux density incident on a surface and coming directly from the solar cone $\Delta\Omega_d$ without any in-scattering contribution, Eq. 2 is substituted into Eq. 1 and simplified since no sources are present in $\mathcal{D}$ and $\partial\mathcal{D}_\mathcal{S}$. In addition, the integral over wavelengths is formulated to account for absorption and scattering coefficient values given as k-distributions (Lacis et al. 1979) in narrow spectral bands. Thus, the integral over wavelengths in Eq. 1 is replaced by a double sum over the numbers of spectral bands N_{bd} and band quadrature points N_{qd} (with quadrature weights $p_{m,q}$, and m is the subscript for a band whereas q is the quadrature index). For the band integration with a quadrature, the quadrature weights are multiplied by the spectral interval ($\lambda_m - \lambda_{m-1}$). This term is reformulated to introduce the PDF p_Λ allowing the algorithm to sample uniformly a wavelength in the band. Furthermore, the integral expression for $\dot{q}_d$ is written with test functions and PDFs (p_{Λ_m}, p_Λ, and p_{Ω_d}) to highlight the underlying backward MCM algorithm:

$$\dot{q}_d(\mathbf{x}_0) = \overbrace{\sum_{m=1}^{N_{bd}} p_{\Lambda_m} \int_{\lambda_{m-1}}^{\lambda_m} p_\Lambda \, d\lambda \sum_{q=1}^{N_{qd}} p_{m,q} \int_{\Delta\Omega_d} p_{\Omega_d} \, d\Omega(\boldsymbol{\omega}_d)}^{\text{samplings}} \Bigg(\mathcal{H}(\mathbf{x}_d \in \partial\mathcal{D}_d) \underbrace{\left\{ \frac{I_d(\mathbf{x}_0, -\boldsymbol{\omega}_d, \lambda)\, |\mathbf{n}(\mathbf{x}_0)\cdot\boldsymbol{\omega}_d|}{p_{\Lambda_m}\, p_\Lambda\, p_{\Omega_d}} \right\}}_{\text{MCM weight}} + \mathcal{H}(\mathbf{x}_d \notin \partial\mathcal{D}_d)\,\{0\} \Bigg), \tag{3}$$

$$I_d(\mathbf{x}_0, -\boldsymbol{\omega}_d, \lambda) = I_{d,ex}(\mathbf{x}_d, -\boldsymbol{\omega}_d, \lambda)\, T_e(\mathbf{x}_0, -\boldsymbol{\omega}_d, \lambda), \tag{4}$$

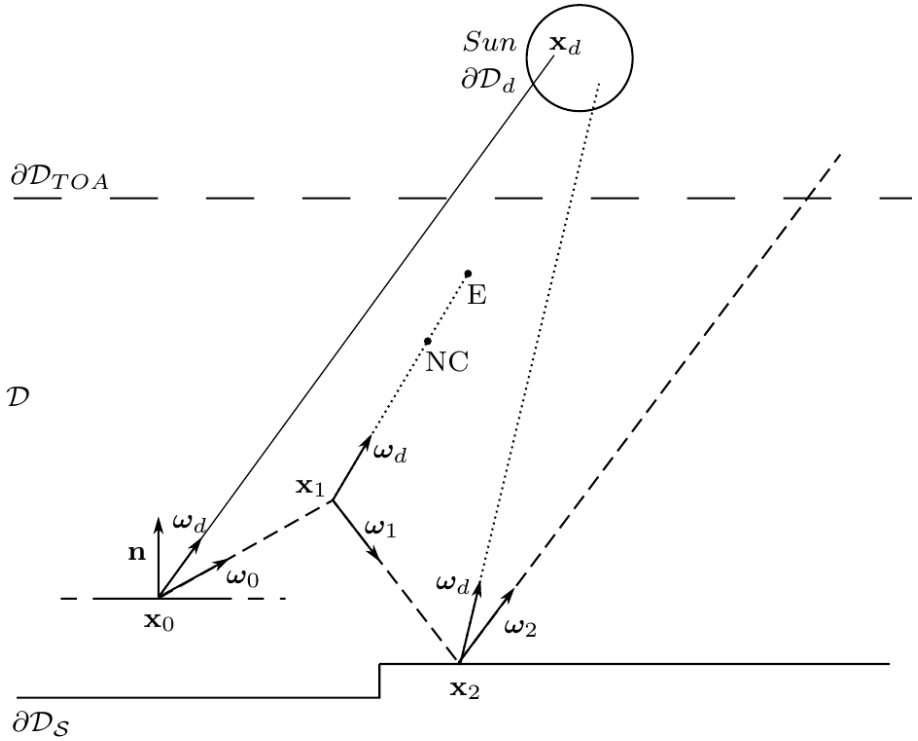

Fig. 1 Representation of possible realizations of the backward MCM algorithm to compute $\dot{q}_d$ and $\dot{q}_{sc}$ with contributory paths considered in the reverse direction (from $\mathbf{x}_0$ to a source). The solid line shows a realization to compute $\dot{q}_d$; the dashed line shows a realization for the computation of $\dot{q}_{sc}$ with a scattering at $\mathbf{x}_1$ and a reflection at $\mathbf{x}_2$ with their unshaded direct contributions in dotted lines that can experience null-collision (NC) and extinction (E) events before reaching TOA

where T_e is the transmissivity by extinction of the monochromatic solar radiation through the atmosphere along a straight line. The integral expression of $\dot{q}_d$ (Eq. 3) was formulated to highlight the MCM algorithm of resolution. Integrals and PDFs were gathered at the beginning showing the different samplings. After sampling the band number, the wavelength, the quadrature point, and the direction into the solar cone, a test of intersection is performed, which will enable recording the MCM weight. The weight of a MCM realization written between braces, $\{\cdot\}$, is selected depending on whether an intersection $\mathbf{x}_d$ occurs in direction $\boldsymbol{\omega}_d$. If an intersection occurs (e.g., $\mathbf{x}_d \in \partial\mathcal{D}_{\mathcal{S}}$) with the geometry surface, the Sun is considered shadowed at $\mathbf{x}_0$ and the realization weight is zero. The PDFs considered

for radiation wavelength and solar direction samplings, respectively, are:

$$p_{\Lambda_m} = \frac{F_{d,ex}(\lambda_{m-1},\lambda_m)}{F_{d,ex}(\lambda_0,\lambda_{N_{bd}})}, \tag{5}$$

$$F_{d,ex}(\lambda_{m-1},\lambda_m) = \frac{\int_{\lambda_{m-1}}^{\lambda_m} I_{d,ex}(\lambda)\,d\lambda}{\int_0^{+\infty} I_{d,ex}(\lambda)\,d\lambda}, \tag{6}$$

$$p_\Lambda = \frac{1}{\lambda_m - \lambda_{m-1}}, \tag{7}$$

$$p_{\Omega_d}(\boldsymbol{\omega}_d) = \frac{1}{\pi\left(1-|\boldsymbol{\omega}_{Sun}\cdot\boldsymbol{\omega}_d|^2\right)}. \tag{8}$$

The spectral band is sampled with a discrete PDF (Eq. 5) whose elements represent the fraction of the Sun's extraterrestrial radiation in the mth spectral band (Eq. 6). To sample a wavelength λ in band m, a uniform PDF is chosen (Eq. 7). Sampling $\boldsymbol{\omega}_d$ is done with PDF p_{Ω_d} (Eq. 8) assuming $I_{d,ex}$ is constant inside the solar disc. Computation of T_e by MCM uses the null-collision technique (evaluated by Galtier et al. 2013, and used by Villefranque et al. 2019) which requires to set (per band) a uniform value of the extinction coefficient $\hat{\beta}$ throughout a volume (such as $\mathcal{D}$) that is greater or equal to the maximum value of β in this volume. For T_e (Eq. 9), the technique consists in sampling the extinction path length with PDF $p_{\hat{\beta}}$ (Eq. 10) using a uniform and maximum value $\hat{\beta}(\lambda) = \beta(\mathbf{x}_j,\lambda)+\beta_n(\mathbf{x}_j,\lambda)$, which is achieved by adding $\beta_n(\mathbf{x}_j,\lambda)$ to compensate for the spatial heterogeneity of $\beta(\mathbf{x}_j,\lambda)$.

$$\begin{aligned} T_e(\mathbf{x}_j,-\boldsymbol{\omega}_d,\lambda) = \int_0^{+\infty} p_{\hat{\beta}}\,d\ell_e \Big(& \mathcal{H}(\ell_e > \|\mathbf{x}_j-\mathbf{x}_{TOA}\|)\,\{1\} + \\ & \mathcal{H}(\ell_e < \|\mathbf{x}_j-\mathbf{x}_{TOA}\|)\Big[P_\beta\,\{0\} + \\ & \underbrace{(1-P_\beta)\;T_e(\mathbf{x}_{j+1},-\boldsymbol{\omega}_d,\lambda)}_{\text{null-collision}}\Big]\Big), \end{aligned} \tag{9}$$

$$p_{\hat{\beta}}(\mathbf{x}_{j+1},\lambda) = \hat{\beta}(\lambda)\exp\Big[-\hat{\beta}(\lambda)\,\ell_e\Big], \tag{10}$$

$$P_\beta(\mathbf{x}_{j+1},\lambda) = \frac{\beta(\mathbf{x}_{j+1},\lambda)}{\hat{\beta}(\lambda)}. \tag{11}$$

In MCM computation of T_e (Eq. 9) and when the extinction event ($\mathbf{x}_{j+1} = \mathbf{x}_j + \boldsymbol{\omega}_d\ell_e$) is beyond TOA, the weight is unity, meaning that the bundle of rays survived. If the event occurs below TOA and it is an actual collision (absorption or scattering) with probability P_β (Eq. 11), the realization weight of T_e is zero. Alternatively, if the event is a null collision with probability $(1-P_\beta)$, a new transmissivity is computed using again Eq. 9 but from the new location $\mathbf{x}_{j+1}$. Thus, a realization of $T_e(\mathbf{x}_j)$ takes the value zero or unity. The null-collision coefficient associated to the extinction (β_n) may produce numerous collisions depending on its value and should be carefully adjusted, such as in the acceleration grids technique of Villefranque et al. (2019) where $\mathcal{D}$ is divided into voxels having their own $\hat{\beta}$ to decrease the number of null collisions.

3.1.2 Scattered Solar Flux Density

The scattered solar radiative flux incident on a surface at $\mathbf{x}_0$ includes all the contributions scattered or reflected at least once and can be formulated as

$$\dot{q}_{sc}(\mathbf{x}_0) = \sum_{m=1}^{N_{bd}} p_{\Lambda_m} \int_{\lambda_{m-1}}^{\lambda_m} p_\Lambda \, d\lambda \sum_{q=1}^{N_{qd}} p_{m,q} \int_{2\pi} p_\Omega \, d\Omega(\boldsymbol{\omega}_0) \times \frac{I_{sc}(\mathbf{x}_0, -\boldsymbol{\omega}_0, \lambda) \, |\mathbf{n}(\mathbf{x}_0) \cdot \boldsymbol{\omega}_0|}{p_{\Lambda_m} \, p_\Lambda \, p_\Omega}. \tag{12}$$

The scattered solar radiative intensity is obtained from a reformulation of Eq. 2 in the framework of the solar intensity splitting approach using a null-collision technique for scattering and the introduction of Lambertian or specular surfaces:

$$\begin{aligned} I_{sc}(\mathbf{x}_j, -\boldsymbol{\omega}_j, \lambda) = \int_0^{+\infty} p_{\hat{\sigma}_s} \, d\ell_{j+1} \, T_a(\mathbf{x}_j, -\boldsymbol{\omega}_j, \lambda, \ell_{j+1}) \Big\{ & \\ \mathcal{H}(\mathbf{x}_{j+1} \in \mathcal{D}) \Big(P_{\sigma_s} \sum_{i=1}^{N_{sp}} P_{\sigma_{s,i}} \Big[\int_{\Delta\Omega_d} p_{\Omega_d} \, d\Omega(\boldsymbol{\omega}_d) \, \{W_{sc,d}\} & \\ + \int_{4\pi} p_i \, d\Omega(\boldsymbol{\omega}_{j+1}) \, I_{sc}(\mathbf{x}_{j+1}, -\boldsymbol{\omega}_{j+1}, \lambda) \Big] & \\ + (1 - P_{\sigma_s}) \, I_{sc}(\mathbf{x}_{j+1}, -\boldsymbol{\omega}_{j+1} = -\boldsymbol{\omega}_j, \lambda) \Big) & \\ + \mathcal{H}(\mathbf{x}_{j+1} \in \partial\mathcal{D}_{\mathcal{S}_L}) \Big(\int_{\Delta\Omega_d} p_{\Omega_d} \, d\Omega(\boldsymbol{\omega}_d) \, \{W_{r,d}\} + & \\ \int_{2\pi} p_L \, d\Omega(\boldsymbol{\omega}_{j+1}) \rho'^{\cap}(\mathbf{x}_{j+1}, \lambda) \, I_{sc}(\mathbf{x}_{j+1}, -\boldsymbol{\omega}_{j+1}, \lambda) \Big) & \\ + \mathcal{H}(\mathbf{x}_{j+1} \in \partial\mathcal{D}_{\mathcal{S}_F}) \, \rho_F(\mathbf{x}_{j+1}, \lambda) \, I_{sc}(\mathbf{x}_{j+1}, -\boldsymbol{\omega}_{j+1}, \lambda) & \\ + \mathcal{H}(\mathbf{x}_{j+1} \in \partial\mathcal{D}_{TOA}) \, \{0\} \Big\}. & \end{aligned} \tag{13}$$

Each segment of the multi-scattered and multi-reflected random path is computed by Eq. 13. This equation involves the scattered radiative intensity, $I_{sc}(\mathbf{x}_{j+1}, -\boldsymbol{\omega}_{j+1}, \lambda)$, but at a different position and direction. This self-invoking expression is adopted to avoid writing the nested integrals whose numbers can be very high. Indeed, a random path may involve a huge number of nested integrals from $j = 0$ to $j = n_{sc} + n_r$ (total number of scattering, n_{sc}, and reflection, n_r, events, respectively). The terms $\{W_{sc,d}\}$ and $\{W_{r,d}\}$ are direct solar contributions at scattering or reflection events (Fig. 1), respectively:

$$W_{sc,d} = \mathcal{H}(\mathbf{x}_d \in \partial\mathcal{D}_d) \, I_d(\mathbf{x}_{j+1}, -\boldsymbol{\omega}_d, \lambda) \, \frac{p_i(\mathbf{x}_{j+1}, -\boldsymbol{\omega}_d | -\boldsymbol{\omega}_j, \lambda)}{p_{\Omega_d}},$$

$$W_{r,d} = \mathcal{H}(\mathbf{x}_d \in \partial\mathcal{D}_d) \, I_d(\mathbf{x}_{j+1}, -\boldsymbol{\omega}_d, \lambda) \, \rho'^{\cap}(\mathbf{x}_{j+1}, \lambda) \, \frac{p_L(\mathbf{x}_{j+1}, -\boldsymbol{\omega}_d)}{p_{\Omega_d}}.$$

Their values are recorded at each scattering or reflection event during the random path and may be zero if the Sun is shadowed (e.g., $\mathbf{x}_d \in \partial\mathcal{D}_{\mathcal{S}}$). In this formulation of the multi-scattered solar radiative intensity I_{sc} (Eq. 13), the random path

inside $\mathcal{D}$ is determined with a null-collision technique and PDF $p_{\hat{\sigma}_s}$ (Eq. 15) that only involves the scattering processes. A maximum and uniform value of the scattering coefficient is assumed such as $\hat{\sigma}_s(\lambda) = \sigma_s(\mathbf{x}_j, \lambda) + \sigma_n(\mathbf{x}_j, \lambda)$ with $\sigma_s(\mathbf{x}_j, \lambda) = \sum_{i=1}^{N_{sp}} \sigma_{s,i}(\mathbf{x}_j, \lambda)$ the sum over the number of species (N_{sp}) of monochromatic scattering coefficients. For an event inside $\mathcal{D}$, i.e., $\mathcal{H}(\mathbf{x}_{j+1} \in \mathcal{D})$, there is a probability P_{σ_s} (Eq. 16) for an actual scattering to occur with one of the N_{sp} species constituting the atmosphere. Once the species is sampled with the probability $P_{\sigma_{s,i}}$ (Eq.17), a solar direct contribution $W_{sc,d}$ is computed and a new scattering direction is sampled with the phase function p_i of this species, which leads to computing I_{sc} from this new location and sampled direction. Alternatively, a null-collision leads to compute I_{sc} from an unchanged direction with Eq. 13. Reaching an opaque surface on $\partial\mathcal{D}_{\mathcal{S}}$, the direct solar contribution $W_{r,d}$ is recorded only for Lambertian surfaces. In this case, a new reflection direction is sampled with PDF p_L (Eq. 18). If a specular surface is intersected, there is no direct solar contribution and the reflection direction is given by the Snell–Descartes' law. It is worth noticing some rare events can affect the convergence. If the last reflection of the path is specular and reflects the Sun, the weight value, $\rho_F\, I_{d,ex}$, is several orders of magnitude greater than for the other realizations. This causes convergence issues and a higher number of realizations is required to achieve an acceptable accuracy on the incident solar flux density. A similar convergence issue is due to the contribution $W_{sc,d}$ that can exhibit high values when $\boldsymbol{\omega}_j$ is almost aligned with $\boldsymbol{\omega}_d$ and when the phase function is highly peaked in the forward direction. When the path reaches TOA, the recursivity stops and all the scattered and reflected direct solar contributions are summed to compute a realization of I_{sc}. The PDFs and probabilities used in the formulation of $\dot{q}_{sc}$ and I_{sc} are given by:

$$p_{\Omega}(\mathbf{x}_j, \boldsymbol{\omega}_j) = \frac{|\mathbf{n}(\mathbf{x}_j) \cdot \boldsymbol{\omega}_j|}{\pi}, \tag{14}$$

$$p_{\hat{\sigma}_s}(\mathbf{x}_{j+1}, \lambda) = \hat{\sigma}_s(\lambda) \exp\Big[- \hat{\sigma}_s(\lambda)\, \ell_{j+1} \Big], \tag{15}$$

$$P_{\sigma_s}(\mathbf{x}_{j+1}, \lambda) = \frac{\sigma_s(\mathbf{x}_{j+1}, \lambda)}{\hat{\sigma}_s(\lambda)}, \tag{16}$$

$$P_{\sigma_{s,i}}(\mathbf{x}_{j+1}, \lambda) = \frac{\sigma_{s,i}(\mathbf{x}_{j+1}, \lambda)}{\sigma_s(\mathbf{x}_{j+1}, \lambda)}, \tag{17}$$

$$p_L(\mathbf{x}_{j+1}, \boldsymbol{\omega}_{j+1}) = \frac{|\mathbf{n}(\mathbf{x}_{j+1}) \cdot \boldsymbol{\omega}_{j+1}|}{\pi}. \tag{18}$$

The transmissivity of radiation by absorption used in Eq. 13 is computed by a null-collision technique with the majorant $\hat{\kappa}(\lambda) = \kappa(\mathbf{x}_{j+1}, \lambda) + \kappa_n(\mathbf{x}_{j+1}, \lambda)$, in the same way as explained previously for the transmissivity by extinction (Eq. 9):

$$T_a(\mathbf{x}_j, -\boldsymbol{\omega}_j, \lambda, \ell_{j+1}) = \int_0^{+\infty} p_{\hat{\kappa}}\, d\ell_a \Big(\mathcal{H}(\ell_a > \ell_{j+1})\{1\} + \mathcal{H}(\ell_a < \ell_{j+1}) \Big[P_\kappa\{0\} + (1 - P_\kappa)\, \{T_a(\mathbf{x}_{j+1}, -\boldsymbol{\omega}_j, \lambda, \ell_{j+1} - \ell_a)\} \Big] \Big),$$

$$p_{\hat{\kappa}}(\ell, \lambda) = \hat{\kappa}(\lambda) \exp\Big[- \hat{\kappa}(\lambda)\, \ell_a \Big],$$

$$P_\kappa = \frac{\kappa(\mathbf{x}_{j+1}, \lambda)}{\hat{\kappa}(\lambda)}.$$

The solar radiative flux density and its associated standard error are estimated with the backward MCM algorithm through N realizations of its random variables:

$$\tilde{\dot{q}}(\mathbf{x}_0) = \tilde{\dot{q}}_d(\mathbf{x}_0) + \tilde{\dot{q}}_{sc}(\mathbf{x}_0) = \frac{1}{N}\sum_{k=1}^{N} W_{\dot{q},k} = \frac{1}{N}\sum_{k=1}^{N}\Big(W_{\dot{q}_d,k} + W_{\dot{q}_{sc},k}\Big),$$

$$\tilde{\sigma}_{\tilde{\dot{q}}} = \frac{1}{\sqrt{N}}\sqrt{\frac{1}{N}\sum_{k=1}^{N} W_{\dot{q},k}^2 - \tilde{\dot{q}}^2}.$$

Replacing I_d in Eq. 3 with Eq. 4 allows one to express the MCM weight (Eq. 27) of the kth realization of the MCM estimate (Eq. 26) for the direct solar flux density. Similarly, introducing Eq. 13 in Eq. 12 leads to the expression of the MCM weight (Eq. 29) of the kth realization of the MCM estimate (Eq. 28) for the diffuse solar flux density. These relations are gathered in Appendix 2. As a result, the MCM algorithm estimating $\tilde{\dot{q}}(\mathbf{x}_0)$ needs to evaluate the sum of the solar direct contribution at $\mathbf{x}_0$ with all the reflected or scattered direct solar contributions along the multiple scattering and reflection random paths.

3.2 Terrestrial Infrared Radiative Flux Density

The infrared radiative flux includes all transmitted radiation originating from thermal sources located at opaque building and vegetation facets as well as inside the semi-transparent cloudy atmosphere. Moreover, each heat source is known because all the temperatures are assumed known inside the scene (gas, particles, buildings, and vegetation). It is assumed that the downwelling terrestrial infrared radiative intensity at TOA is zero. The infrared radiative flux density incident on a surface at $\mathbf{x}_0$ may be written as:

$$\dot{q}_{ir}(\mathbf{x}_0) = \sum_{m=1}^{N_{bd}} p_{\Lambda_m}^{ir} \int_{\lambda_{m-1}}^{\lambda_m} p_\Lambda \, d\lambda \sum_{q=1}^{N_{qd}} p_{m,q} \int_{2\pi} p_\Omega \, d\Omega(\boldsymbol{\omega}_0) \times \frac{I_{ir}(\mathbf{x}_0, -\boldsymbol{\omega}_0, \lambda)\, |\mathbf{n}(\mathbf{x}_0)\cdot\boldsymbol{\omega}_0|}{p_{\Lambda_m}^{ir}\, p_\Lambda\, p_\Omega},$$

where I_{ir} is the infrared radiative intensity and $p_{\Lambda_m}^{ir}$ the band sampling PDF driven by the Planck's distribution law with F_b the black-body fraction:

$$p_{\Lambda_m}^{ir} = \frac{F_b(\lambda_m, T) - F_b(\lambda_{m-1}, T)}{F_b(\lambda_{N_{bd}}, T) - F_b(\lambda_0, T)},$$

$$F_b(\lambda_m, T) = \frac{1}{\int_0^\infty I_b(T,\lambda)\, d\lambda} \int_0^{\lambda_m} I_b(T,\lambda)\, d\lambda.$$

The expression of I_{ir} (Eq. 19) includes nested integrals through new infrared intensities coming from other locations and directions. The radiative path made of multiple scattering and reflections is build with a backward MCM algorithm from the end point ($\mathbf{x}_0$) to the source. Thus, an absorption event in the backward algorithm corresponds to its emission location. This formulation holds because the local thermodynamic equilibrium is assumed at the reflection, scattering, and absorption/emission points. After sampling the wavelength (m and λ), the quadrature

point, the direction ($\boldsymbol{\omega}_0$), and an extinction length (ℓ_{j+1}), the type of extinction event is sampled inside domain $\mathcal{D}$, between absorption (P^{ir}_{κ}), scattering ($P^{ir}_{\sigma_s}$), or null-collision. If a bundle of rays hits either a Lambertian ($\partial\mathcal{D}_{\mathcal{S}_L}$) or a specular ($\partial\mathcal{D}_{\mathcal{S}_F}$) surface, a Bernoulli trial is conducted to choose between a reflection or an absorption event:

$$
\begin{aligned}
I_{ir}(\mathbf{x}_j,-\boldsymbol{\omega}_j,\lambda) = \int_0^{+\infty} p_{\hat{\beta}}\, d\ell_{j+1} \Big\{ & \\
& \mathcal{H}(\mathbf{x}_{j+1}\in\mathcal{D})\Big(P^{ir}_{\kappa} \sum_{i=1}^{N_{sp}} P_{\kappa_i}\left\{I_b\big(T(\mathbf{x}_{j+1}),\lambda\big)\right\} + \\
& \quad P^{ir}_{\sigma_s} \sum_{i=1}^{N_{sp}} P_{\sigma_{s,i}} \int_{4\pi} p_i\, d\Omega(\boldsymbol{\omega}_{j+1})\, I_{ir}(\mathbf{x}_{j+1},-\boldsymbol{\omega}_{j+1},\lambda) \\
& \quad + (1-P^{ir}_{\kappa}-P^{ir}_{\sigma_s})\, I_{ir}(\mathbf{x}_{j+1},-\boldsymbol{\omega}_{j+1}=-\boldsymbol{\omega}_j,\lambda)\Big) \\
& + \mathcal{H}(\mathbf{x}_{j+1}\in\partial\mathcal{D}_{\mathcal{S}_L})\Big(P^{ir}_{\varepsilon}\left\{I_b\big(T(\mathbf{x}_{j+1}),\lambda\big)\right\} + \\
& \quad (1-P^{ir}_{\varepsilon}) \int_{2\pi} p_L\, d\Omega(\boldsymbol{\omega}_{j+1})\, I_{ir}(\mathbf{x}_{j+1},-\boldsymbol{\omega}_{j+1},\lambda)\Big) \\
& + \mathcal{H}(\mathbf{x}_{j+1}\in\partial\mathcal{D}_{\mathcal{S}_F})\Big(P^{ir}_{\varepsilon}\left\{I_b\big(T(\mathbf{x}_{j+1}),\lambda\big)\right\} + \\
& \quad (1-P^{ir}_{\varepsilon})\, I_{ir}(\mathbf{x}_{j+1},-\boldsymbol{\omega}_{j+1},\lambda)\Big) \\
& + \mathcal{H}(\mathbf{x}_{j+1}\in\partial\mathcal{D}_{TOA})\left\{0\right\}\Big\}.
\end{aligned}
\tag{19}
$$

At each collision (scattering, reflection, or null-collision) a new infrared intensity is computed with Eq. 19. At the endpoint of the reverse radiative path, where an absorption event occurs, a black-body intensity is saved to compute the MCM weight. The detailed expressions of probabilities introduced in Eq. 19 are given by:

$$
\begin{aligned}
P^{ir}_{\kappa}(\mathbf{x}_{j+1},\lambda) &= \frac{\kappa(\mathbf{x}_{j+1},\lambda)}{\hat{\beta}(\lambda)}, \\
P_{\kappa_i}(\mathbf{x}_{j+1},\lambda) &= \frac{\kappa_i(\mathbf{x}_{j+1},\lambda)}{\kappa(\mathbf{x}_{j+1},\lambda)}, \\
P^{ir}_{\sigma_s}(\mathbf{x}_{j+1},\lambda) &= \frac{\sigma_s(\mathbf{x}_{j+1},\lambda)}{\hat{\beta}(\lambda)}, \\
P^{ir}_{\varepsilon}(\mathbf{x}_{j+1},-\boldsymbol{\omega}_j,\lambda) &= 1-\rho'^{\cap}(\mathbf{x}_{j+1},\boldsymbol{\omega}_j,\lambda).
\end{aligned}
\tag{20}
$$

The total infrared radiative flux density (Eq. 30) is estimated with the backward MCM algorithm through N realizations of the random variable $W_{\dot{q}_{ir}}$ (see Appendix 2, Eq. 31). Thus, the backward MCM algorithm consists in exploring the geometry from $\mathbf{x}_0$ with a radiative random walk and averaging contributions proportional to the black-body radiative flux emitted at endpoints.

4 Data and Boundary Conditions

The solar spectrum irradiance ($I_{d,ex}$) is obtained by averaging the data of year 2020 from the dataset of Coddington et al. (2015). The solar constant value is set to 1360.45 $\mathrm{W\,m^{-2}}$ (Coddington et al. 2016), which leads to a value of 1359.89 +/− 0.0019 $\mathrm{W\,m^{-2}}$ when integrated with the present MCM algorithm over the spectral range of the radiative properties, i.e., between 200 and 12195.1 nm (or 820-50000 $\mathrm{cm^{-1}}$). The user can specify the Sun's half angle to account for the variation of apparent solar disc radius due to change in Earth–Sun distance.

The European Centre for Medium-Range Weather Forecasts (ECMWF) Radiation Scheme (ECRAD) is used to produce the atmospheric profiles of temperature, species, and spectral radiative properties (Hogan et al. 2016). The 1D atmospheric profile is taken from Hogan and Bozzo (2018) and computed by ECRAD software (Hogan and Bozzo 2016) where the clouds are removed (liquid water and ice contents are set to zero) producing clear-sky conditions for the simulations. Originally, this atmosphere was the three-dimensional large-eddy simulation of cumulus cloud field from Stevens et al. (1999) which was used in the International Intercomparison of three-dimensional Radiation Codes (I3RC) of Cahalan et al. (2005). The k-distributions of the gas radiative properties are generated with an implementation of the Rapid Radiative Transfer Model for Global Circulation Models (RRTMG) in ECRAD which is based on the Line-by-Line Radiative Transfer Model (LBLRTM) (Clough et al. 2005).

The spectral radiative properties of the diffuse surfaces are obtained from the Spectral Library of impervious Urban Materials (SLUM) available from the London Urban Micromet data Archive (LUMA) (Kotthaus et al. 2013). These spectral data were measured by a portable Fourier transform infrared spectrometer to retrieve the solar reflectivity and the infrared emissivity (Kotthaus et al. 2014). Reflectivity of specular window glasses are computed with the complex refractive index from Rubin (1985) in solar and infrared spectral ranges. Each surface material may be set to a different but constant temperature for the simulation of infrared radiative fluxes.

The urban geometry made of different land materials (streets, grass, water, etc.), building types with different facets (walls, windows, roofs, etc.), and trees (opaque trunks and leaves) is computed with an in-house procedural city generator.

Figure 2 displays a rendering in the visible part of the solar spectrum of a procedurally generated city. The same city geometry is repeated infinitely (Fig. 2a), a variety of building types with different materials is taken into account (Fig. 2b), the windows are made of specularly reflecting glass (Fig. 2c), tree leaves and trunks are represented explicitly (Fig. 2d). The rendering is made with the same MCM-based radiative transfer code that is used for the calculation of solar radiative flux density (Sect. 3.1).

5 Validation of Monte Carlo Models

Both MCM models for solar and infrared radiative fluxes are validated against the results of the radiosity method for the infinitely long street-canyon geometry (Sect. 5.1). Then, a comparison between the results of MCM and the radiosity method is presented in street-canyon geometry with multiple reflections (Sect. 5.2).

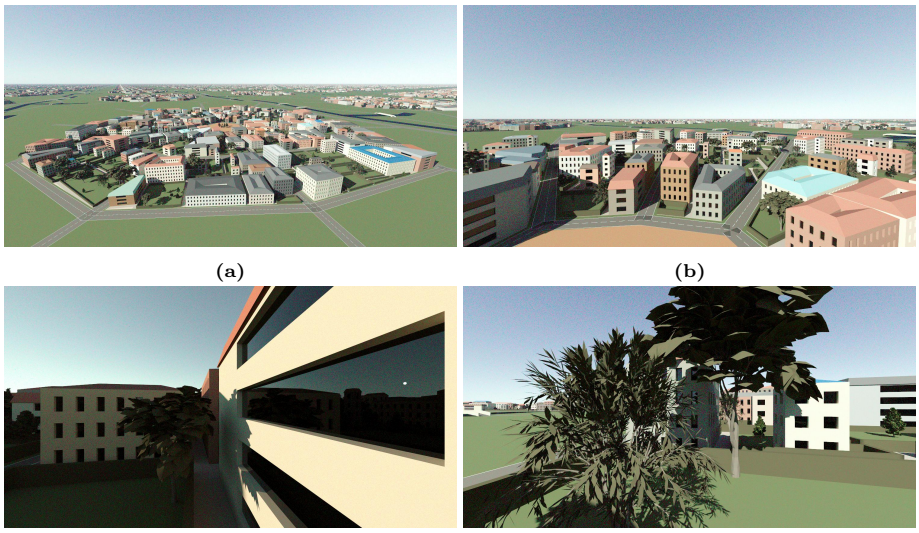

Fig. 2 Rendering in the visible part of the solar spectrum of a procedurally generated city for clear-sky conditions with a variety of materials from the SLUM database, trees, and spectrally reflecting windows. The number of pixels is 1500 × 800, the vertical field of view 70°, and the number of samples per pixel 200 (a), (b), (d), and 1000 (c) which is required due to the variance created by the spectral reflection of the direct solar radiation by the window

In addition, the closure of the urban solar radiation budget (Sect. 5.3) is checked in various urban complex three-dimensional geometries.

5.1 Monte Carlo Validation for Street Canyon Geometry

The MCM urban radiation model is validated for the infinitely long street-canyon urban geometry against results of the urban canopy model Town Energy Balance (TEB, Masson 2000) which calculates radiative exchange with the radiosity method. Analytical expressions of radiative fluxes exist for the special case of an infinitely long street canyon with no variety in building height, opaque broadband Lambertian materials, and neither atmospheric scattering nor absorption (Noilhan 1981; Masson 2000). These expressions are coded in TEB and Redon et al. (2017) compared the TEB results for a selection of street canyons with those of the SOLENE model showing good performance of TEB. We therefore take TEB results as a benchmark for evaluating numerically the results provided by the newly developed MCM model. An important restriction is that TEB does not mesh the urban facets (road, wall, and roof), but calculates only one radiative observable per facet (e.g., the direct solar radiation absorbed by the road). This means that if one part of the road is shaded and the other part sunlit, the radiation that is reflected by the road will be considered by TEB as being reflected with equal probability from each point of the road whereas the MCM model will follow the track of each reflected bundle of rays from its actual reflection location. Differences between the MCM model and TEB will therefore appear for a reflecting

Table 1 Characteristics of the infinitely long street-canyon urban morphologies employed for the validation of the MCM radiation model. For all geometries, the building height (H) is 10 m, and the plan area building density (λ_p) is 0.5.

Aspect ratio	Road width [m]
0.1	100
0.2	50
0.5	20
1.0	10
2.0	5
5.0	2
10.0	1

road (wall) for low (high) aspect ratio (building height divided by street width) of the street canyon. Idealized street canyon morphologies with aspect ratios ranging from 0.1 to 10 are created (Table 1). They all have the same building height (H = 10 m) and plan area building density ($\lambda_p = 0.5$), but differ in street width and wall surface density (λ_w). In this specific case, the aspect ratio is equal to λ_w. Two idealized boundary conditions for downwelling solar radiation are analyzed: 1) direct-only downwelling solar radiation with a solar elevation angle of 45°; 2) diffusive-only downwelling solar radiation. The diffusive-only simulations are similar to downwelling solar radiation for a completely overcast sky with optically thick clouds. For the direct-only simulations, the apparent radius of the solar disc in the MCM model is set to 10^{-5} rd to match the point-like Sun assumption by TEB (collimated solar radiation). Atmospheric scattering and absorption are not included in the MCM model to match the TEB assumptions. TEB results represent the average for all solar azimuth angles, in other words the distribution of street orientation is uniform. To be comparable with TEB, mean surface (S) fluxes averaged on the Sun's azimuth angle (φ), $\dot{Q}_S$ (Eq. 21), will be computed by MCM based on local flux densities ($\dot{q}$) defined previously:

$$\begin{aligned} \dot{Q}_S &= \int_0^{2\pi} p_\varphi \, d\varphi \int_S p_S \, ds(\mathbf{x}) \, \lambda_S \, \varepsilon(\mathbf{x}) \, \dot{q}(\mathbf{x}), \\ p_\varphi &= \frac{1}{2\pi}, \\ p_S &= \frac{1}{S}, \end{aligned} \tag{21}$$

with λ_S the corresponding surface density which is $\lambda_p = 0.5$ for the roof and the road, and equal to the aspect ratio for the walls ($\lambda_w = H/W$). Three combinations of road and wall albedo are considered (the roof is purely absorbing): 1) case REFWALL, only the walls reflect radiation with a broadband albedo of 0.5 (road and roof albedo are zero); 2) case REFROAD, only the road reflects radiation with a broadband albedo of 0.5 (walls and roof albedo are zero); 3) case SPEC-REFROAD, only the road reflects radiation with a spectrally varying albedo corresponding to the white weathered concrete C006 taken from the SLUM database (Kotthaus et al. 2014) (walls and roof albedo are zero). TEB cannot take into account a spectral albedo. Therefore, the effective broadband albedo of the road ($\overline{\rho}_R^{\prime\cap}$) to be used by TEB is calculated by a spectral average weighted by the

solar radiation:

$$\overline{\rho}_R'^{\cap} = \frac{1}{\int I_d(\lambda)\, d\lambda} \int \rho_R'^{\cap}(\lambda)\, I_d(\lambda)\, d\lambda.$$

With this road albedo, TEB and MCM results should be similar. The MCM is used to calculate the mean and standard error of up- and downwelling solar flux above the street canyon ($\dot{Q}_U$, $\dot{Q}_D$), and the solar flux absorbed by the roof, walls, and road ($\dot{Q}_{F,a}$, $\dot{Q}_{W,a}$, $\dot{Q}_{R,a}$) with $N = 10^7$. Results of solar radiation budget for different aspect ratios are presented in Fig. 3 for REFWALL and REFROAD cases with normalized radiative flux (and their standard errors) by $\dot{Q}_D$. For RE-

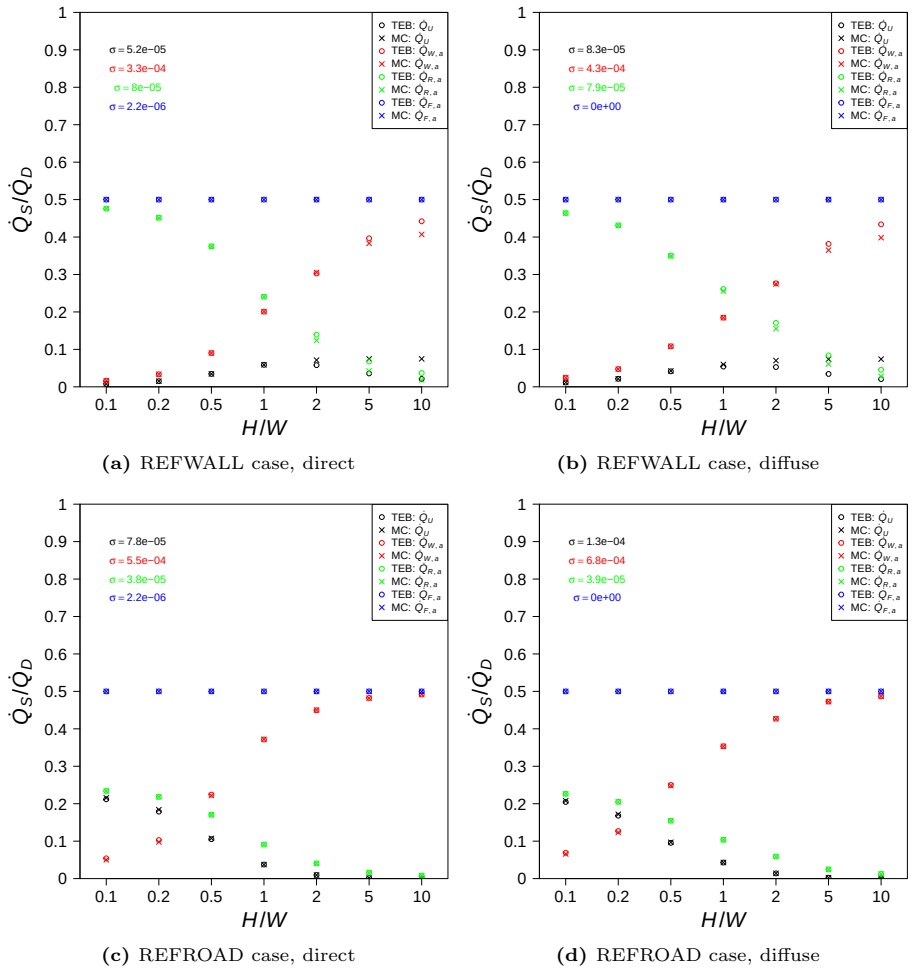

(a) REFWALL case, direct

(b) REFWALL case, diffuse

(c) REFROAD case, direct

(d) REFROAD case, diffuse

Fig. 3 Solar radiation budget of an infinitely long street canyon with opaque broadband Lambertian materials simulated with TEB and MCM for REFWALL and REFROAD cases with either direct- or diffuse-only downwelling solar irradiation. The values denoted with σ display the maximum value of the normalized standard error of the different terms of the budget for all aspect ratios

FWALL, only walls reflect radiation and the upwelling flux tends to increase with the aspect ratio. For REFROAD, the road reflects and the upwelling flux increases when the road width increases (and the aspect ratio decreases). In both cases, the absorbed flux by the walls increases with the aspect ratio. Indeed, when the road width is narrowing, the aspect ratio is increasing and more irradiation is intercepted by the walls. Conversely, the absorbed flux by the road decreases when the aspect ratio increases because of the shadowing by walls. In addition, the non-linear profiles of $\dot{Q}_{W,a}$ and $\dot{Q}_{R,a}$ are due to effects of multiple reflections. $\dot{Q}_{W,a}$ is slightly higher for the REFROAD case, because reflected radiation from the road is intercepted by the walls. Similarly, higher values of $\dot{Q}_{R,a}$ are reached in the REFWALL case where the road receives reflections from the walls. In all cases $\dot{Q}_{F,a}$ has a constant value of 0.5 because building density λ_p is 0.5 and the roof is absorbing all the downwelling radiation. For REFWALL (Fig. 3a, b), MCM and TEB results agree almost perfectly for aspect ratios below 1. For higher aspect ratios, discrepancies appear, which are due to the TEB assumption of uniform radiosity on large surfaces that fails to catch the effects of localized irradiation and shadowing. In the MCM calculation, more solar radiation is reflected by the upper part of the wall favouring reflection towards the sky compared to TEB that assumes solar radiation is reflected uniformly on the surface leading to a larger interception by the opposite wall. This explains why TEB simulates less upwelling radiation than the MCM model and consequently higher absorbed fluxes ($\dot{Q}_{W,a}$ and $\dot{Q}_{R,a}$). No large differences are found between the results obtained with the direct-only (Fig. 3a) and diffusive-only downwelling radiation boundary conditions (Fig. 3b). Normalized absorbed solar fluxes by the road ($\dot{Q}_{R,a}/\dot{Q}_D$) are slightly smaller for direct-only solar radiation compared to diffusive-only, which is plausible since direct radiation is more likely to be intercepted by walls than diffusive radiation. For REFROAD (Fig. 3c, d), the MCM and TEB results agree almost perfectly for high aspect ratios and small discrepancies appear for low aspect ratios. The MCM simulates slightly higher upwelling radiation values than TEB and consequently slightly lower absorbed fluxes. With MCM, the shaded part of the road is close to the shadowed wall. Thus, the reflected radiation from the road is less absorbed by the shadowed wall leading to slightly higher upwelling flux. The comparison of TEB and MCM in the REFWALL and REFROAD cases (Fig. 3) shows that the MCM reproduces the results of TEB when the uniform surface radiosity assumption of TEB is not limiting. Moreover, those results highlight the ability of the developed MCM algorithm to account for directional dependency and manage radiative flux computation in complex geometry. The results for SPEC-REFROAD are displayed in Fig. 4. In this case, MCM accounts for the spectral dependency of road albedo ($\rho_R'^{\cap}$) whereas TEB uses a constant broadband albedo ($\overline{\rho}_R'^{\cap}$). Given that the wall absorbs perfectly, there are no multiple reflections in the street canyon geometry, hence no difference between MCM and TEB can be expected from the albedo treatment. Results of Fig. 4 confirm this expectation and they are considered as a numerical validation of the MCM spectral sampling. Similarly to Fig. 3c, d, the TEB and MCM results agree almost perfectly for the high aspect ratios.

In addition to solar flux comparisons, the MCM algorithm validation in the terrestrial infrared is studied with a comparison to TEB results for averaged net

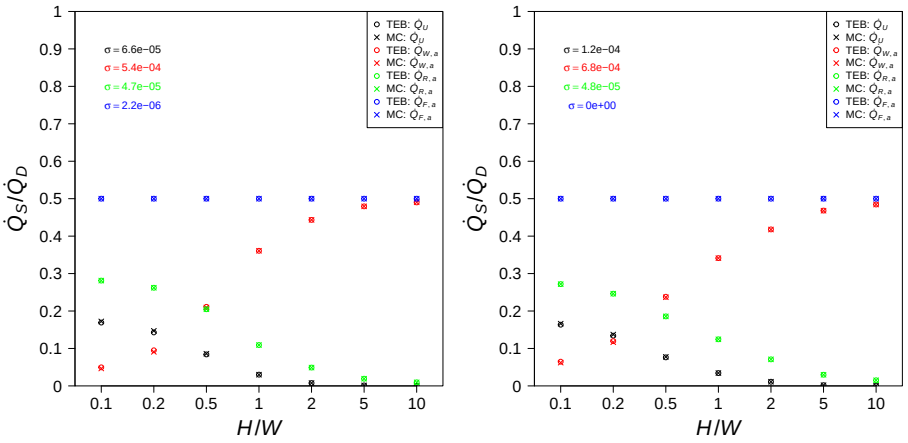

(a) SPEC-REFROAD case, direct **(b)** SPEC-REFROAD case, diffuse

Fig. 4 Solar radiation budget of an infinitely long street canyon simulated with TEB and MCM radiation models for SPEC-REFROAD case. The values denoted with σ display the maximum value of the normalized standard error of the different terms for all aspect ratios

exchanged radiative (NER) fluxes between a surface and its surroundings:

$$\dot{E}_S = \int_0^{2\pi} p_\varphi \, d\varphi \int_S p_S \, ds(\mathbf{x}) \, \lambda_S \, \varepsilon(\mathbf{x}) \, \left(\sigma_{SB} \, T^4(\mathbf{x}) - \dot{q}_{ir}(\mathbf{x}) \right), \tag{22}$$

with σ_{SB} the Stefan–Boltzmann constant and ε the surface emissivity assumed isotropic and grey. Two combinations of opaque road and wall emissivities are considered while the roof has a constant emissivity $\varepsilon = 0.5$: 1) case IR-REFWALL, the walls reflect radiation with a broadband albedo of 0.5 and the road albedo is zero; 2) case IR-REFROAD, the road reflects radiation with a broadband albedo of 0.5 and the walls' albedo are zero. For these cases, the sky temperature is set to $T_{sky} = 273.15$ K and the street-canyon surface temperatures are isothermal at 300 K. Thus, the NER flux will be negative for the sky and positive for the street-canyon surfaces that lose energy by radiation towards the sky directly or via multiple reflections. The MCM is used to calculate the mean and standard error of NER fluxes for the sky, the roof, the walls, and the road ($\dot{E}_{sky}$, $\dot{E}_F$, $\dot{E}_W$, $\dot{E}_R$) with $N = 10^7$. MCM and TEB results of NER fluxes, normalized by the constant downwelling flux from the sky ($\dot{Q}_D = \sigma_{SB} {T_{sky}}^4$), are presented in Fig. 5 for different aspect ratios and cases IR-REFWALL (Fig. 5a) and IR-REFROAD (Fig. 5b). For both cases, $\dot{E}_F$ is constant whatever the aspect ratio, while $\dot{E}_W$ increases and $\dot{E}_R$ decreases with the aspect ratio. Indeed, as H/W increases the road width and its view factor to the sky decrease. For low aspect ratio, values of $\dot{E}_R$ are higher for the IR-REFWALL since road emissivity is one compared to the IR-REFROAD case where road emissivity is 0.5. The increase of wall NER fluxes ($\dot{E}_W$) with H/W is due to the greater influence of the wall density augmentation compared to the decrease in view factor values of an individual vertical wall towards the sky. MCM results give higher $\dot{E}_R$ and $\dot{E}_W$ than TEB which is again due to the multiple reflections. Indeed, the absorption is overestimated by TEB due

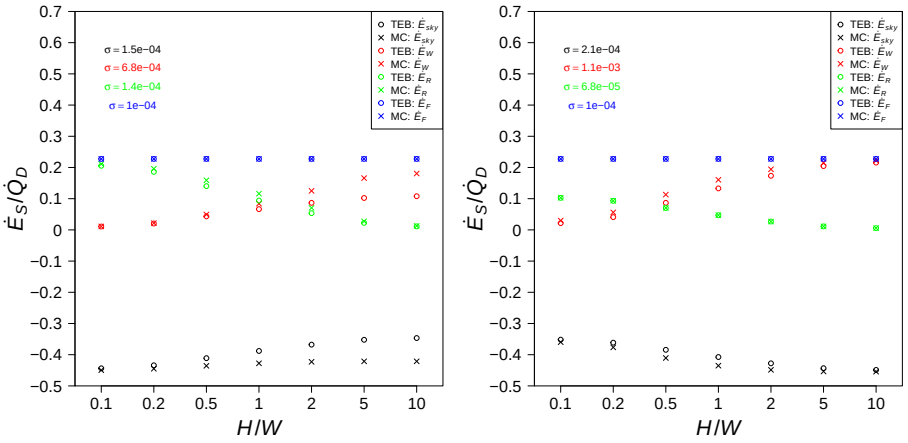

(a) IR-REFWALL case **(b)** IR-REFROAD case

Fig. 5 NER fluxes between a surface and its surroundings in infinitely long street canyons with opaque broadband Lambertian materials simulated with TEB and MCM for IR-REFWALL and IR-REFROAD cases. The values denoted with σ display the maximum value of the normalized standard error of the NER fluxes for all aspect ratios

to the uniform radiosity assumption, which leads to lower NER fluxes (Eq. 22) compared to MCM.

5.2 Results for Street-Canyon Geometry with Multiple Reflections

The effects of multiple reflections on radiative flux densities are studied in street-canyon geometries. Assuming all walls are grey, opaque, and Lambertian with an albedo of 0.5, results from TEB and MCM are compared (Fig. 6) in two cases: 1) the ALLREF case for solar direct (Fig. 6a) and diffuse (Fig. 6b) radiative flux densities normalized with the downwelling solar flux; 2) the IR-ALLREF case for NER fluxes (Fig. 6c) normalized by $\dot{Q}_D = \sigma_{SB} {T_{sky}}^4$ with a sky temperature set to $T_{sky} = 273.15$ K and uniform street-canyon surface temperatures at 300 K.

The behaviour of ALLREF results for $\dot{Q}_{F,a}$, $\dot{Q}_{R,a}$, and $\dot{Q}_{W,a}$ follow the ones of Fig. 3a and 3b where only the walls reflect. However, in case ALLREF, values of $\dot{Q}_{F,a}$ and $\dot{Q}_{R,a}$ are lower due the albedo difference, whereas $\dot{Q}_{W,a}$ values are similar. Thus, the multiple reflections lead $\dot{Q}_U$ to decrease when the aspect ratio increases. Some discrepancies are found between MCM and TEB due to the overestimation of wall absorption by TEB.

The results of case IR-ALLREF are similar to the one with reflecting walls only (IR-REFWALL, Fig. 5a). The uniform radiosity assumption in TEB causes an overestimation of wall absorption and leads to lower values of $\dot{E}_W$ compared to MCM.

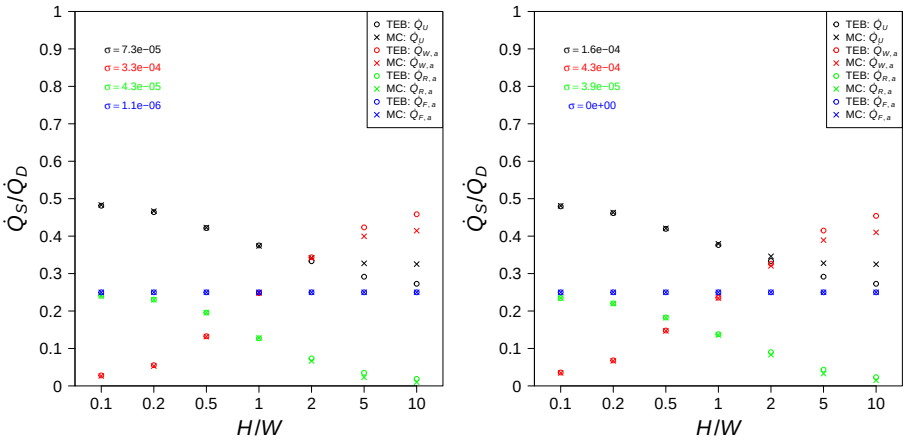

(a) ALLREF case, direct **(b)** ALLREF case, diffuse

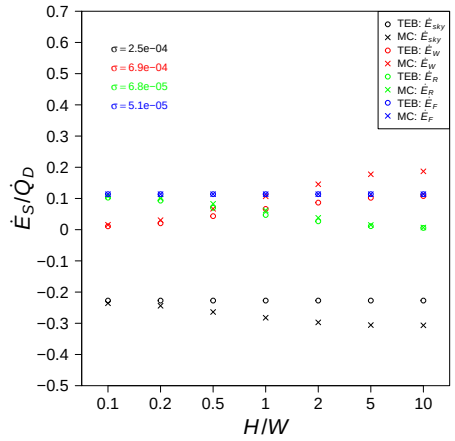

(c) IR-ALLREF case

Fig. 6 Solar and infrared radiation budgets of infinitely long street canyons with opaque broadband Lambertian materials simulated with TEB and MCM for ALLREF and IR-ALLREF cases; The values denoted with σ display the maximum value of the normalized standard error of the different terms of the budget for all aspect ratios

5.3 Closure of Urban Solar Radiation Budget

The closure of the urban solar radiation budget in urban geometries with different degrees of complexity is investigated. First, infinite street canyon morphologies like in Sect. 5.1 with opaque broadband Lambertian ($\overline{\rho}'^{\cap} = 0.5$) or spectral C006 materials are considered. The same direct-only and diffusive-only boundary conditions are used as in Sect. 5.1. The solar radiation budget consists of $\dot{Q}_U$, $\dot{Q}_D$, $\dot{Q}_{F,a}$, $\dot{Q}_{W,a}$, and $\dot{Q}_{R,a}$. The MCM model is used to calculate the mean and standard error of all these terms. The residual of the solar radiation budget normalized

Table 2 Standard errors of the residual, $\tilde{\sigma}_{\Delta}$ (1), for the urban solar radiation budget obtained with different number of realizations (N) and for infinitely long street canyons with different aspect ratios with direct-only downwelling solar radiation. All surfaces are composed of opaque broadband Lambertian materials with albedo equal to 0.5

Aspect ratio	$N = 1 \times 10^5$	$N = 1 \times 10^6$	$N = 1 \times 10^7$
0.1	4.6×10^{-4}	1.4×10^{-4}	4.5×10^{-5}
0.2	6.3×10^{-4}	2.0×10^{-4}	6.3×10^{-5}
0.5	9.2×10^{-4}	2.9×10^{-4}	9.2×10^{-5}
1.0	1.1×10^{-3}	3.4×10^{-4}	1.1×10^{-4}
2.0	1.4×10^{-3}	4.4×10^{-4}	1.4×10^{-4}
5.0	2.2×10^{-3}	7.3×10^{-4}	2.3×10^{-4}
10.0	3.4×10^{-3}	1.1×10^{-3}	3.4×10^{-4}

by the downwelling radiation (Δ) is given by

$$\Delta = 1 - \frac{\tilde{\dot{Q}}_U + \tilde{\dot{Q}}_{F,a} + \tilde{\dot{Q}}_{W,a} + \tilde{\dot{Q}}_{R,a}}{\tilde{\dot{Q}}_D}.$$

Given that all terms of the solar radiation budget have been calculated independently, the uncertainty propagation law can be used to calculate the dimensionless standard error of the residual, $\tilde{\sigma}_{\Delta}$, based on the standard errors of the different observables:

$$\tilde{\sigma}_{\Delta} = \Bigg[\left(\frac{\partial \Delta}{\partial \tilde{\dot{Q}}_D} \right)^2 \tilde{\sigma}^2_{\tilde{\dot{Q}}_D} + \left(\frac{\partial \Delta}{\partial \tilde{\dot{Q}}_U} \right)^2 \tilde{\sigma}^2_{\tilde{\dot{Q}}_U} + \left(\frac{\partial \Delta}{\partial \tilde{\dot{Q}}_{F,a}} \right)^2 \tilde{\sigma}^2_{\tilde{\dot{Q}}_{F,a}} + \left(\frac{\partial \Delta}{\partial \tilde{\dot{Q}}_{W,a}} \right)^2 \tilde{\sigma}^2_{\tilde{\dot{Q}}_{W,a}} + \left(\frac{\partial \Delta}{\partial \tilde{\dot{Q}}_{R,a}} \right)^2 \tilde{\sigma}^2_{\tilde{\dot{Q}}_{R,a}} \Bigg]^{\frac{1}{2}}.$$

MCM simulations have been made for $N = 1 \times 10^5$, $N = 1 \times 10^6$, and $N = 1 \times 10^7$. Table 2 presents the results for broadband Lambertian materials and direct-only solar radiation. Very good convergence is found for this simple urban morphology. For $N = 1 \times 10^7$, the values of $\tilde{\sigma}_{\Delta}$ are almost exactly a factor of 10 lower than for $N = 1 \times 10^5$. The values in Table 2 are also useful to determine how many MCM realizations are required to obtain a desired accuracy of results. For most applications, uncertainties below 1% could be sufficient, thus the computationally very efficient $N = 1 \times 10^5$ could be used since $3\,\tilde{\sigma}_{\Delta} \leq 0.01$. The convergence for diffusive-only downwelling radiation and/or Lambertian spectral materials is very similar (not shown). For diffusive-only radiation, the values of $\tilde{\sigma}_{\Delta}$ are higher than for direct-only, therefore with $N = 1 \times 10^5$, the value of $3\,\tilde{\sigma}_{\Delta}$ becomes higher than 0.01 for aspect ratios of 5 and 10. For such geometries, $N = 1 \times 10^6$ is therefore recommended.

The analysis of the solar radiation budget closure is repeated for more complex urban geometries displayed in Fig. 7. Three types of urban geometries are considered which correspond to the Local Climate Zones (LCZ, Stewart and Oke 2012), Sparsely built (LCZ9, $\lambda_p = 0.11$, $\lambda_w = 0.23$, $H_m = 5.8\,\mathrm{m}$, $\sigma_H = 1.4\,\mathrm{m}$; Fig. 7a, b), Compact mid rise (LCZ2, $\lambda_p = 0.53$, $\lambda_w = 1.21$, $H_m = 16.1\,\mathrm{m}$, $\sigma_H = 3.9\,\mathrm{m}$; Fig. 7c, d), and Compact high rise (LCZ1, $\lambda_p = 0.46$, $\lambda_w = 6.62$, $H_m = 86.2\,\mathrm{m}$,

$\sigma_H = 15.1\,\mathrm{m}$; Fig. 7e, f). Two different configurations of urban materials are considered: NOWINDOWS and WINDOWS. For NOWINDOWS (Fig. 7a, c, e), all roofs are made of rusting cement red roofing tiles R008, walls and windows of white weathered concrete C006, and all ground surfaces of black tarmac asphalt A009. The surfaces are Lambertian and the spectral albedo is taken from the SLUM dataset (Kotthaus et al. 2014). For WINDOWS, the roof, wall, and ground materials are the same as for NOWINDOWS, except the window glazing is assumed to be made of soda lime silica glass. The spectral complex refractive index is obtained from Rubin (1985) to compute the directional and spectral specular reflectivity. The glazing ratio is 0.3 for all geometries.

The results for NOWINDOWS are displayed in Table 3. Good convergence is

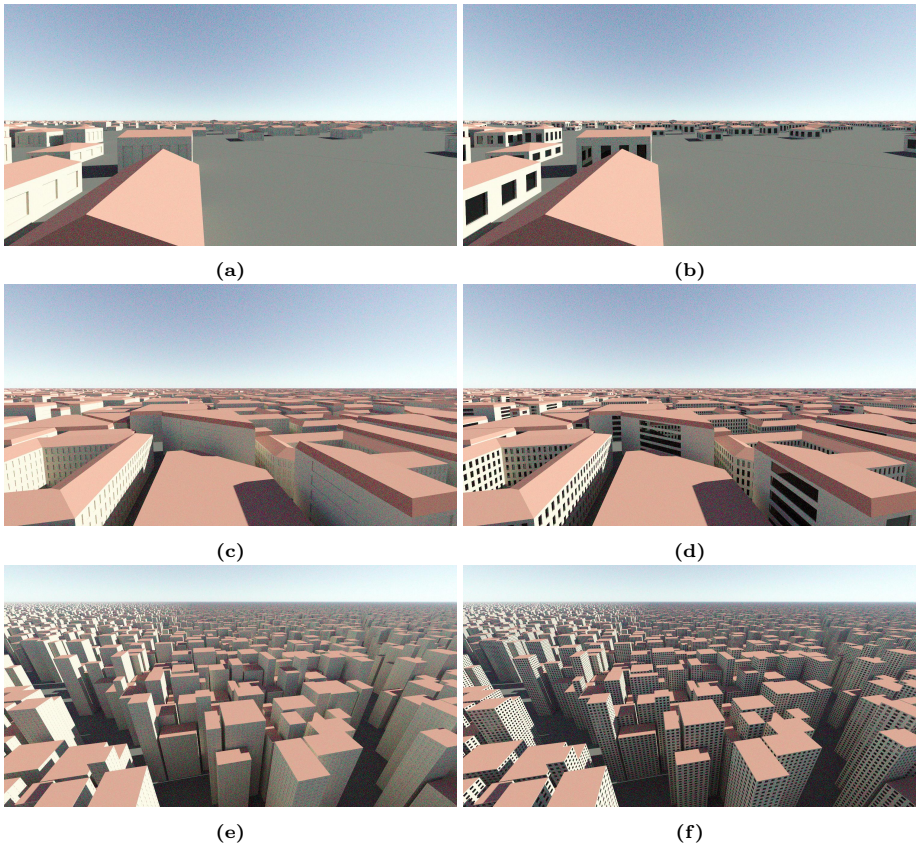

Fig. 7 Rendering in the visible part of the solar spectrum of three types of urban geometries (LCZ, Stewart and Oke (2012)) with (b, d, f) and without (a, c, e) glazing window; (a, b): LCZ9; (c, d): LCZ2; (e, f): LCZ1. The number of pixels is 1500 × 800, the vertical field of view 70°, and the number of samples per pixel is 200

found for all urban geometries and solar irradiations. The lowest values of $\tilde{\sigma}_{\Delta}$ are found for LCZ9 while the highest are found for LCZ1 geometry. The convergence depends on the number of reflections that increases with the building density and

Table 3 Standard errors of the residual, $\tilde{\sigma}_{\Delta}$ (1), for the urban solar radiation budget obtained with different number of realizations (N) for realistic urban geometries without glazing windows (NOWINDOWS)

Urban morphology	$N = 1 \times 10^5$	$N = 1 \times 10^6$	$N = 1 \times 10^7$
LCZ9, direct-only	8.5×10^{-4}	2.7×10^{-4}	8.5×10^{-5}
LCZ2, direct-only	1.4×10^{-3}	4.4×10^{-4}	1.4×10^{-4}
LCZ1, direct-only	3.1×10^{-3}	9.7×10^{-4}	3.1×10^{-4}
LCZ9, diffusive-only	1.3×10^{-3}	4.0×10^{-4}	1.3×10^{-4}
LCZ2, diffusive-only	1.8×10^{-3}	5.8×10^{-4}	1.8×10^{-4}
LCZ1, diffusive-only	3.7×10^{-3}	1.2×10^{-3}	3.7×10^{-4}

Table 4 Standard errors of the residual, $\tilde{\sigma}_{\Delta}$ (1), for the urban solar radiation budget obtained with different number of realizations (N) for realistic urban geometries with glazing windows (WINDOWS)

Urban morphology	$N = 1 \times 10^5$	$N = 1 \times 10^6$	$N = 1 \times 10^7$
LCZ9, direct-only	8.4×10^{-4}	4.6×10^{-4}	5.7×10^{-4}
LCZ2, direct-only	1.4×10^{-3}	2.9×10^{-3}	1.9×10^{-3}
LCZ1, direct-only	3.1×10^{-3}	7.7×10^{-3}	3.9×10^{-3}
LCZ9, diffusive-only	1.3×10^{-3}	4.0×10^{-4}	1.3×10^{-4}
LCZ2, diffusive-only	1.8×10^{-3}	5.8×10^{-4}	1.8×10^{-4}
LCZ1, diffusive-only	3.8×10^{-3}	1.2×10^{-3}	3.8×10^{-4}

aspect ratio. Thus, for complex geometry, more MCM realizations are needed to achieve a similar confidence interval on the solution.

The results for WINDOWS are displayed in Table 4. For diffusive-only radiation, the values of $\tilde{\sigma}_{\Delta}$ are very close to those obtained for NOWINDOWS. The spectrally reflecting windows do not cause convergence issues for diffusive-only radiation. For direct-only radiation, the values of $\tilde{\sigma}_{\Delta}$ in the WINDOWS case are similar to those of NOWINDOWS only for $N = 1 \times 10^5$. However, their values are higher for higher number of realizations. This is due to rare events caused by specular reflection of solar radiative intensity (see Sect. 3.1.2). Although the standard errors do not follow a decrease proportional to $\frac{1}{\sqrt{N}}$, increasing the number of realizations still compensates the loss of precision. The use of a rather high number of realizations (e.g., $N = 1 \times 10^7$) is therefore strongly recommended for urban geometries containing spectrally reflecting windows.

6 Conclusions and Outlook

The present article has introduced a new reference model for urban radiative transfer, which takes into account complex building and vegetation geometries with a variety of spectrally and potentially specularly reflecting materials. The radiative transfer in the cloudy and polluted atmosphere above the city is also taken into account. This model is solved by a backward MCM algorithm using null-collision technique and importance sampling. Previously developed null-collision algorithms make the radiative transfer calculation time almost independent of the atmospheric composition and cloud content. Furthermore, the added urban-related complexity of three-dimensional geometry, spectral and directional properties does

not lead to an increase of the computation time. The main advantages of this new MCM model are its capability to represent the full complexity of urban geometry without leading to prohibitively high computational cost and that it does represent the relevant physical processes, e.g., scattering and absorption of radiation due to potentially cloudy or polluted air in-between the buildings, spectral urban material reflectivity, and specularly reflecting materials like windows. The new MCM model has been validated successfully for infinitely long street-canyon geometries against the radiosity-based radiation model included in the urban land surface model TEB. The closure of the solar radiation budget for urban geometries of different complexity has been investigated and it has been found that for simple geometries like a street canyon or cities similar to LCZ9 (sparsely built), LCZ2 (compact mid rise), and LCZ1 (compact high rise) with Lambertian materials, a number of MCM realizations of 1×10^5 to 1×10^6 is sufficient to calculate the urban solar radiation budget with an accuracy of 1%, which might be sufficient for most applications. In the case specularly reflecting windows are considered, the MCM algorithm converges much slower due to the variance introduced by the specular reflection of solar radiative intensity. The use of at least 1×10^7 MCM realizations is recommended for such geometries.

Future use of the MCM model is planned with two main purposes. First, the MCM model can be used to quantify the radiation budget of buildings or humans by taking into account the full complexity of the geometry and physical processes. This intended application can help to better design cities in order to reduce building energy consumption or improve human thermal comfort, which is important for climate change mitigation and adaptation. The MCM model could also be applied to rural areas, especially forests. For this application however, realistic and detailed geometries of individual trees as well as the positioning of trees with respect to each other (e.g., in a forest) need to be known. A first step would be to work with the actual canopies scenes included in the Fifth Phase of the RAdiation transfer Model Intercomparison (RAMI) initiative. Secondly, the MCM model can be used as a reference to quantify the uncertainties of urban radiative transfer models that simplify the geometric complexity or the physical processes. For example, the error introduced by the very common infinite street-canyon geometry employed by most urban land surface models can be investigated for different urban geometries. Obstacle-resolving meteorological models employ the radiosity method to calculate radiative exchange since it is computationally cheap. The new MCM model can be used to analyze the uncertainty that arises from neglecting atmospheric scattering and absorption in different meteorological conditions. Finally, this MCM algorithm may be used in novel combined heat transfer models (Villefranque et al. 2022) to evaluate the impact of climate change and the effect of mitigation and adaptation measures at urban scales.

Acknowledgements Simone Kotthaus and Sue Grimmond are acknowledged for sharing the Spectral Library of impervious Urban Materials, which is included in the presented MCM model. Robin Hogan is acknowledged for his help on the calculation of the atmospheric radiative properties using ECRAD, and Valéry Masson for his guidance on radiative exchange calculation in TEB.

Appendix 1: Principles of the Monte Carlo Method to Solve Integrals

The MCM is a stochastic numerical technique to compute integrals based on using sequences of random numbers (Dupree and Fraley 2002; Delatorre et al. 2014; Howell et al. 2020). Let S be the integral of a function f over a multiple dimension domain $\mathcal{D}$ (Eq. 23). The steps to compute S via the MCM are as follows:

- to introduce a non-zero PDF p over $\mathcal{D}$ (Eq. 23),
- to formulate S as the expectation of $W = \frac{f(X)}{p(X)}$, where X is a random variable distributed according to p,
- to sample numerically a large number N of realizations x_1, x_2, ..., x_N of the random variable X, according to the selected PDF p, and with a random number r generated with a uniform PDF in $[0; 1)$ (Eq. 24),
- to compute the MCM weight $W_k = \frac{f(x_k)}{p(x_k)}$ for each realization x_k,
- to retain the mean value for numerical estimation $\tilde{S}$ of S (Eq. 25),

$$S = \int_D f(x)\, dx = \int_D p(x)\, \frac{f(x)}{p(x)}\, dx = E\left(\frac{f(X)}{p(X)}\right) = E(W), \tag{23}$$

$$r = \int_{-\infty}^{x} p(x)\, dx, \tag{24}$$

$$S \approx \tilde{S} = \frac{1}{N} \sum_{k=1}^{N} W_k(x_k). \tag{25}$$

As an example, let's compute the total emissive power of an opaque surface M and chose p_Ω (Eq. 14) as the PDF. In this context of radiative transfer, generic Eq. 23 is replaced by

$$\begin{aligned} M(\vec{y}) &= \int_{2\pi} \varepsilon'(\vec{y}, \vec{\omega})\; I_b(\vec{y})\; |\vec{n} \cdot \vec{\omega}|\; d\Omega(\vec{\omega}), \\ &= \int_{2\pi} p_\Omega(\vec{\omega})\; \frac{\varepsilon'(\vec{y}, \vec{\omega})\; I_b(\vec{y})\; |\vec{n} \cdot \vec{\omega}|}{p_\Omega(\vec{\omega})}\; d\Omega(\vec{\omega}), \\ &= \int_0^{2\pi} p_\varphi\; d\varphi \int_0^{\frac{\pi}{2}} p_\theta\; d\theta\; \{W\}, \end{aligned}$$

with ε' the surface directional emissivity and where W is the random variable of the MCM weight computed with the realization θ_i and φ_i of their corresponding random variable following their PDF, p_θ and p_φ, respectively. These PDFs and the variable realizations are obtained using a representation of the solid angle with spherical coordinates (θ is the normal angle and φ the azimuth angle),

$$p_\Omega\; d\Omega = p_\Omega\; |\sin\theta|\; d\theta\; d\varphi = p_\theta\; d\theta\; p_\varphi\; d\varphi,$$

and using Eq. 24, a realization of θ and ϕ may be obtained:

$$\begin{aligned} \theta_k &= \sin^{-1}\sqrt{r_k}, \\ \varphi_k &= 2\,\pi\, r_k. \end{aligned}$$

The MCM weight saved at each realization has the following expression:

$$W_k = \frac{\varepsilon'(\vec{y},\vec{\omega})\ I_b(\vec{y})\ |\cos\theta_k\ \sin\theta_k|}{p_\varphi\ p_\theta} = \pi\ \varepsilon'(\vec{y},\vec{\omega}(\theta_k,\varphi_k))\ I_b(\vec{y}).$$

The sampling of θ_k and φ_k allows one to compute W_k. Evaluating a large number of times (N times) the MCM weight computation and then averaging their values (Eq. 25) will produce a MCM estimate ($\tilde{M}$) of the emissive power.

To evaluate the convergence of a MCM estimate $\tilde{S}$, an associated standard error value $\tilde{\sigma}_{\tilde{S}}$ may be computed with the standard deviation of the MCM weight (σ_W) based on the statistically independent samples of the N realizations:

$$\tilde{\sigma}_{\tilde{S}} = \frac{\sigma_W}{\sqrt{N}},$$

where,

$$\sigma_W = \sqrt{\left(\frac{1}{N}\sum_{k=1}^{N} W_k^2\right) - \tilde{S}^2}.$$

As a rule of thumb, a MCM estimate with an associated standard error verifying $\frac{3\,\tilde{\sigma}_{\tilde{S}}}{\tilde{S}} \leq 0.01$ is considered converged for most applications in radiative transfer. However, this rule fails when the standard error shows a low value and the computation is not converged because rare events are not taken into account. This risk may occur if N is too small to sample rare events whereas they can contribute significantly to the estimate.

Appendix 2: Monte Carlo Estimates, Weights, and Standard Errors

The MCM estimate, weight, and standard error for the direct solar radiative flux density are given by

$$\tilde{\tilde{q}}_d(\mathbf{x}_0) = \frac{1}{N}\sum_{k=1}^{N} W_{\dot{q}_d,k}, \tag{26}$$

$$W_{\dot{q}_d,k} = \mathcal{H}(\mathbf{x}_d \in \partial\mathcal{D}_d)\,\mathcal{H}(\ell_e > \|\mathbf{x}_0 - \mathbf{x}_{TOA}\|)\,\frac{I_{d,ex}\,|\mathbf{n}(\mathbf{x}_0)\cdot\boldsymbol{\omega}_d|}{p_{\Lambda_m}\ p_\Lambda\ p_{\Omega_d}}, \tag{27}$$

$$\tilde{\sigma}_{\tilde{q}_d} = \frac{1}{\sqrt{N}}\sqrt{\frac{1}{N}\sum_{k=1}^{N} W_{\dot{q}_d,k}^2 - \tilde{\tilde{q}}_d^2}.$$

The MCM estimate, weight, and standard error for the diffuse solar radiative flux density are given by

$$\tilde{\dot{q}}_{sc}(\mathbf{x}_0) = \frac{1}{N}\sum_{k=1}^{N} W_{\dot{q}_{sc},k}, \tag{28}$$

$$\begin{aligned} W_{\dot{q}_{sc},k} = \frac{|\mathbf{n}(\mathbf{x}_0)\cdot\boldsymbol{\omega}_0|\; I_{d,ex}}{p_{\Lambda_m}\, p_{\Lambda}\, p_{\Omega}\, p_{\Omega_d}} \Bigg(\prod_{j=1}^{n_r} \Big[\mathcal{H}(\mathbf{x}_j \in \partial\mathcal{D}_{\mathcal{S}_L})\, \rho'^{\cap}(\mathbf{x}_j,\lambda) + \\ \mathcal{H}(\mathbf{x}_j \in \partial\mathcal{D}_{\mathcal{S}_F})\, \rho_F(\mathbf{x}_j,\lambda) \Big] \Bigg) \Bigg(\prod_{j=1}^{n_{sc}} \mathcal{H}(\ell_a > \ell_j) \Bigg) \Bigg(\\ \sum_{j=1}^{n_{sc}} \mathcal{H}(\mathbf{x}_j \in \mathcal{D})\, \mathcal{H}(\mathbf{x}_d \in \partial\mathcal{D}_d)\, \mathcal{H}(\ell_e > \|\mathbf{x}_j - \mathbf{x}_{TOA}\|)\, p_i(\mathbf{x}_j, \boldsymbol{\omega}_d | \boldsymbol{\omega}_{j-1}, \lambda) \\ + \sum_{j=1}^{n_r} \mathcal{H}(\mathbf{x}_j \in \partial\mathcal{D}_{\mathcal{S}_L})\, \mathcal{H}(\mathbf{x}_d \in \partial\mathcal{D}_d)\, \mathcal{H}(\ell_e > \|\mathbf{x}_j - \mathbf{x}_{TOA}\|)\, p_L(\mathbf{x}_j, \boldsymbol{\omega}_d) \\ + \mathcal{H}(\mathbf{x}_{n_r} \in \partial\mathcal{D}_{\mathcal{S}_F}) \mathcal{H}(\mathbf{x}_d \in \partial\mathcal{D}_d)\, \mathcal{H}(\ell_e > \|\mathbf{x}_j - \mathbf{x}_{TOA}\|)\, p_{\Omega_d} \Bigg), \end{aligned} \tag{29}$$

$$\tilde{\sigma}_{\tilde{\dot{q}}_{sc}} = \frac{1}{\sqrt{N}} \sqrt{\frac{1}{N}\sum_{k=1}^{N} W^2_{\dot{q}_{sc},k} - \tilde{\dot{q}}^2_{sc}}.$$

In Eq. 29, the total number of events was separated into scattering (n_{sc}) and reflection (n_r) events.

The MCM estimate, weight and standard error for the total infrared radiative flux density are given by

$$\tilde{\dot{q}}_{ir}(\mathbf{x}_0) = \frac{1}{N}\sum_{k=1}^{N} W_{\dot{q}_{ir},k}, \tag{30}$$

$$W_{\dot{q}_{ir},k} = \frac{\pi\, I_b\big(T(\mathbf{x}_{j+1}),\lambda\big)}{p^{ir}_{\Lambda_m}\, p_{\Lambda}}\, \mathcal{H}(\mathbf{x}_{j+1} \in \mathcal{D} \cup \partial\mathcal{D}_{\mathcal{S}_L} \cup \partial\mathcal{D}_{\mathcal{S}_F}), \tag{31}$$

$$\tilde{\sigma}_{\tilde{\dot{q}}_{ir}} = \frac{1}{\sqrt{N}} \sqrt{\frac{1}{N}\sum_{k=1}^{N} W^2_{\dot{q}_{ir},k} - \tilde{\dot{q}}^2_{ir}},$$

where $\mathbf{x}_{j+1}$ is the final position of the random radiative path considered as the emission location.

Declarations

Funding This work received financial support from the French Agency for Ecological Transition ADEME (project MODRADURB-1917C001). Partial financial supports were received from UPPA-E2S Initiatives Grants and from French National Research Agency through grant ANR-21-CE46-0013.

Conflicts of Interest Authors C. Caliot, R. Schoetter and T.-Y. Chung certify that they have no affiliations with or involvement in any organization or entity with any financial interest or non-financial interest in the subject matter or materials discussed in this manuscript. Authors V. Eymet and V. Forest declare they receive salary from company Meso-Star SAS.

Code Availability The new htrdr-urban code package for solar and infrared radiative flux computations associated with the current submission is publicly available at https://gitlab.com/edstar/htrdr/-/tree/main_urban.

Data Availability The data that replicates the findings of this study are publicly available at https://zenodo.org/record/6370467.

References

Aguerre JP, Fernández E, Beckers B (2019) Importance-driven approach for reducing urban radiative exchange computations. Building Simulation 12(2):231–246, DOI 10.1007/s12273-018-0482-4

Akbari H, Pomerantz M, Taha H (2001) Cool surfaces and shade trees to reduce energy use and improve air quality in urban areas. Solar Energy 70(3):295–310, DOI 10.1016/S0038-092X(00)00089-X

Ali-Toudert F, Mayer H (2006) Numerical study on the effects of aspect ratio and orientation of an urban street canyon on outdoor thermal comfort in hot and dry climate. Build Environ 41(2):94–108, DOI 10.1016/j.buildenv.2005.01.013

Ali-Toudert F, Mayer H (2007a) Effects of asymmetry, galleries, overhanging façades and vegetation on thermal comfort in urban street canyons. Solar Energy 81(6):742–754, DOI 10.1016/j.solener.2006.10.007

Ali-Toudert F, Mayer H (2007b) Thermal comfort in an east–west oriented street canyon in Freiburg (Germany) under hot summer conditions. Theor Appl Climatol 87(1):223–237, DOI 10.1007/s00704-005-0194-4

Arnfield AJ (2003) Two decades of urban climate research: a review of turbulence, exchanges of energy and water, and the urban heat island. Int J Climatol 23(1):1–26, DOI 10.1002/joc.859

Bruse M, Fleer H (1998) Simulating surface–plant–air interactions inside urban environments with a three dimensional numerical model. Environ Modell Softw 13(3):373–384, DOI 10.1016/S1364-8152(98)00042-5

Cahalan RF, Oreopoulos L, Marshak A, Evans KF, Davis AB, Pincus R, Yetzer KH, Mayer B, Davies R, Ackerman TP, Barker HW, Clothiaux EE, Ellingson RG, Garay MJ, Kassianov E, Kinne S, Macke A, O'hirok W, Partain PT, Prigarin SM, Rublev AN, Stephens GL, Szczap F, Takara EE, Várnai T, Wen G, Zhuravleva TB (2005) The I3RC: Bringing together the most advanced radiative transfer tools for cloudy atmospheres. Bull Am Meteorol Soc 86(9):1275 – 1294, DOI 10.1175/BAMS-86-9-1275

Clough S, Shephard M, Mlawer E, Delamere J, Iacono M, Cady-Pereira K, Boukabara S, Brown P (2005) Atmospheric radiative transfer modeling: a summary of the AER codes. J Quant Spectrosc Radiat Transf 91(2):233–244, DOI 10.1016/j.jqsrt.2004.05.058

Coddington O, Lean LJ, Doug L, Pilewskie P, Snow M, NOAA CDR Program (2015) NOAA climate data record (CDR) of solar spectral irradiance (SSI), NRLSSI version 2. [ssi_v02r01_yearly_s1610_e2020_c20210204.nc]. DOI 10.7289/V51J97P6

Coddington O, Lean JL, Pilewskie P, Snow M, Lindholm D (2016) A solar irradiance climate data record. Bull Am Meteorol Soc 97(7):1265 – 1282, DOI 10.1175/BAMS-D-14-00265.1

Coelho PJ (2002) The role of ray effects and false scattering on the accuracy of the standard and modified discrete ordinates methods. J Quant Spectrosc Radiat Transf 73:231–238

Collins M, Knutti R, Arblaster J, Dufresne JL, Fichefet T, Friedlingstein P, Gao X, Gutowski W, Johns T, Krinner G, Shongwe M, Tebaldi C, Weaver A, Wehner M (2013) Chapter 12 - long-term climate change: Projections, commitments and irreversibility. In: IPCC (ed) Climate Change 2013: The Physical Science Basis. IPCC Working Group I Contribution to AR5, Cambridge University Press, Cambridge

Delatorre J, Baud G, Bézian J, Blanco S, Caliot C, Cornet J, Coustet C, Dauchet J, El Hafi M, Eymet V, Fournier R, Gautrais J, Gourmel O, Joseph D, Meilhac N, Pajot A, Paulin M, Perez P, Piaud B, Roger M, Rolland J, Veynandt F, Weitz S (2014) Monte Carlo advances and concentrated solar applications. Solar Energy 103:653–681, DOI 10.1016/j.solener.2013.02.035

Dissegna MA, Yin T, Wei S, Richards D, Grêt-Regamey A (2019) 3-D reconstruction of an urban landscape to assess the influence of vegetation in the radiative budget. Forests 10(8), DOI 10.3390/f10080700

Dupree SA, Fraley SK (2002) Monte Carlo Sampling Techniques, Springer US, Boston, MA, pp 21–56. DOI 10.1007/978-1-4419-8491-3-2

El Hafi M, Blanco S, Dauchet J, Fournier R, Galtier M, Ibarrart L, Tregan JM, Villefranque N (2021) Three viewpoints on null-collision monte carlo algorithms. Journal of Quantitative Spectroscopy and Radiative Transfer 260:107,402, DOI https://doi.org/10.1016/j.jqsrt.2020.107402

Farmer JT, Howell JR (1998) Comparison of Monte Carlo strategies for radiative transfer in participating media. Adv Heat Transf 31:333–429, DOI 10.1016/S0065-2717(08)70243-0

Frayssinet L, Merlier L, Kuznik F, Hubert JL, Milliez M, Roux JJ (2018) Modeling the heating and cooling energy demand of urban buildings at city scale. Renew Sust Energ Rev 81:2318–2327, DOI 10.1016/j.rser.2017.06.040

Galtier M, Blanco S, Caliot C, Coustet C, Dauchet J, El Hafi M, Eymet V, Fournier R, Gautrais J, Khuong A, Piaud B, Terrée G (2013) Integral formulation of null-collision Monte Carlo algorithms. J Quant Spectrosc Radiat Transf 125:57–68, DOI 10.1016/j.jqsrt.2013.04.001

Gastellu-Etchegorry JP (2008) 3D Modeling of satellite spectral images, radiation budget and energy budget of urban landscapes. Meteorol Atmos Phys MAP-0/939:1–21, DOI 10.1007/s00703-008-0344-1

Gastellu-Etchegorry JP, Yin T, Lauret N, Cajgfinger T, Gregoire T, Grau E, Feret JB, Lopes M, Guilleux J, Dedieu G, Malenovský Z, Cook BD, Morton D, Rubio J, Durrieu S, Cazanave G, Martin E, Ristorcelli T (2015) Discrete Anisotropic Radiative Transfer (DART 5) for modeling airborne and satellite spectroradiometer and LIDAR acquisitions of natural and urban landscapes. Remote Sens 7(2):1667–1701, DOI 10.3390/rs70201667

Grimmond CSB, Blackett M, Best MJ, Barlow J, Baik JJ, Belcher SE, Bohnenstengel SI, Calmet I, Chen F, Dandou A, Fortuniak K, Gouvea ML, Hamdi R, Hendry M, Kawai T, Kawamoto Y, Kondo H, Krayenhoff ES, Lee SH, Loridan T, Martilli A, Masson V, Miao S, Oleson K, Pigeon G, Porson A, Ryu YH, Salamanca F, Shashua-Bar L, Steeneveld GJ, Tombrou M, Voogt J, Young D, Zhang N (2010) The International Urban Energy Balance Models Comparison Project: First results from Phase 1. J Appl Meteorol Clim 49(6):1268 – 1292, DOI 10.1175/2010JAMC2354.1

Grimmond CSB, Blackett M, Best MJ, Baik JJ, Belcher SE, Beringer J, Bohnenstengel SI, Calmet I, Chen F, Coutts A, Dandou A, Fortuniak K, Gouvea ML, Hamdi R, Hendry M, Kanda M, Kawai T, Kawamoto Y, Kondo H, Krayenhoff ES, Lee SH, Loridan T, Martilli A, Masson V, Miao S, Oleson K, Ooka R, Pigeon G, Porson A, Ryu YH, Salamanca F, Steeneveld G, Tombrou M, Voogt JA, Young DT, Zhang N (2011) Initial results from Phase 2 of the International Urban Energy Balance Model Comparison. Int J Climatol 31(2):244–272, DOI 10.1002/joc.2227

Hogan RJ (2019a) An exponential model of urban geometry for use in radiative transfer applications. Boundary-Layer Meteorol pp 357–372

Hogan RJ (2019b) Flexible treatment of radiative transfer in complex urban canopies for use in weather and climate models. Boundary-Layer Meteorol 173(1):53–78, DOI 10.1007/s10546-019-00457-0

Hogan RJ, Bozzo A (2016) ECRAD: A new radiation scheme for the IFS. ECMWF Technical Memoranda (787)

Hogan RJ, Bozzo A (2018) A flexible and efficient radiation scheme for the ECMWF model. J Adv Model Earth Syst 10(8):1990–2008, DOI https://doi.org/10.1029/2018MS001364

Hogan RJ, Schäfer SAK, Klinger C, Chiu JC, Mayer B (2016) Representing 3-D cloud radiation effects in two-stream schemes: 2. Matrix formulation and broadband evaluation. J Geophys Res Atmos 121:8583–8599, DOI 10.1002/2016JD024875

Howell JR (1998) The Monte Carlo Method in Radiative Heat Transfer. J Heat Transf 120(3):547–560, DOI 10.1115/1.2824310

Howell JR, Mengüç MP, Daun K, Siegel R (2020) Thermal Radiation Heat Transfer (7th ed.). CRC Press, DOI 10.1201/9780429327308

Ko Y (2013) Urban form and residential energy use: A review of design principles and research findings. J Plan Lit 28(4):327–351, DOI 10.1177/0885412213491499

Kotthaus S, Smith T, Wooster M, Grimmond S (2013) Spectral Library of Impervious Urban Materials (version 1.0) [luma_slum_sw.csv luma_slum_ir.csv]

Kotthaus S, Smith TE, Wooster MJ, Grimmond C (2014) Derivation of an urban materials spectral library through emittance and reflectance spectroscopy. ISPRS J Photogramm Remote Sens 94:194–212, DOI 10.1016/j.isprsjprs.2014.05.005

Krayenhoff ES, Christen A, Martilli A, Oke TR (2014) A multi-layer radiation model for urban neighbourhoods with trees. Boundary-Layer Meteorol 151(1):139–178, DOI 10.1007/s10546-013-9883-1

Krč P, Resler J, Sühring M, Schubert S, Salim MH, Fuka V (2021) Radiative Transfer Model 3.0 integrated into the PALM model system 6.0. Geosci Model Dev 14(5):3095–3120, DOI 10.5194/gmd-14-3095-2021

Lacis AA, Wang W, Hansen JE (1979) Correlated k-distribution method for radiative transfer in climate models: Application to effect of cirrus clouds on climate. In: Rev PS (ed) NASA. Goddard Space Flight Center 4th NASA Weather and Climate

Landier L, Gastellu-Etchegorry JP, Ahmad AB, Chavanon E, Lauret N, Feigenwinter C, Mitraka Z, Chrysoulakis N (2018) Calibration of urban canopies albedo and 3D shortwave radiative budget using remote-sensing data and the DART model. Eur J Remote Sens 51(1):739–753, DOI 10.1080/22797254.2018.1462102

Lindsay N, Libois Q, Badosa J, Migan-Dubois A, Bourdin V (2020) Errors in PV power modelling due to the lack of spectral and angular details of solar irradiance inputs. Sol Energy 197:266–278, DOI 10.1016/j.solener.2019.12.042

Masson V (2000) A physically-based scheme for the urban energy budget in atmospheric models. Boundary-Layer Meteorol 94(3):357–397, DOI 10.1023/A:1002463829265

Masson V, Bonhomme M, Salagnac JL, Briottet X, Lemonsu A (2014) Solar panels reduce both global warming and urban heat island. Front Environ Sci 2:1–10

Meso-Star (2021) htrdr 0.6.1: The Monte-Carlo radiative transfer simulator. https://www.meso-star.com/projects/htrdr/htrdr.html

Miguet F, Groleau D (2002) A daylight simulation tool for urban and architectural spaces-application to transmitted direct and diffuse light through glazing. Build Environ 37(8-9):833–843

Milliez M (2006) Micrometeorological modelling in urban areas : pollutant dispersion and radiative effects modelling. Dissertation, Ecole des Ponts ParisTech, France

Modest M (2003) Radiative Heat Transfer - Third Edition. Elsevier Academic Press

Moonen P, Defraeye T, Dorer V, Blocken B, Carmeliet J (2012) Urban physics: effect of the micro-climate on comfort, health and energy demand. Front Archit Res 1(3):197–228, DOI 10.1016/j.foar.2012.05.002

Morille B, Lauzet N, Musy M (2015) SOLENE-microclimate: A tool to evaluate envelopes efficiency on energy consumption at district scale. Enrgy Proced 78:1165–1170, DOI 10.1016/j.egypro.2015.11.088

Morrison W, Kotthaus S, Grimmond C, Inagaki A, Yin T, Gastellu-Etchegorry JP, Kanda M, Merchant CJ (2018) A novel method to obtain three-dimensional urban surface temperature from ground-based thermography. Remote Sens Environ 215:268–283, DOI 10.1016/j.rse.2018.05.004

Morrison W, Yin T, Lauret N, Guilleux J, Kotthaus S, Gastellu-Etchegorry JP, Norford L, Grimmond S (2020) Atmospheric and emissivity corrections for ground-based thermography using 3D radiative transfer modelling. Remote Sens Environ 237:111,524, DOI 10.1016/j.rse.2019.111524

Morrison W, Kotthaus S, Grimmond S (2021) Urban surface temperature observations from ground-based thermography: intra- and inter-facet variability. Urban Clim 35:100,748, DOI 10.1016/j.uclim.2020.100748

Musy M, Malys L, Morille B, Inard C (2015) The use of SOLENE-microclimat model to assess adaptation strategies at the district scale. Urban Clim 14:213–223, DOI 10.1016/j.uclim.2015.07.004

Noilhan J (1981) A model for the net total radiation flux at the surfaces of a building. Build Environ 16(4):259–266, DOI 10.1016/0360-1323(81)90004-4

Oke TR (1982) The energetic basis of the urban heat island. Q J R Meteorol Soc 108(455):1–24, DOI 10.1002/qj.49710845502

Qu Y, Milliez M, Musson-Genon L, Carissimo B (2011) Micrometeorological modeling of radiative and convective effects with a building-resolving code. J Appl Meteorol Clim 50(8):1713 – 1724, DOI 10.1175/2011JAMC2620.1

Redon EC, Lemonsu A, Masson V, Morille B, Musy M (2017) Implementation of street trees within the solar radiative exchange parameterization of TEB in SURFEX v8.0. Geosci Model Dev 10(1):385–411, DOI 10.5194/gmd-10-385-2017

Resler J, Krč P, Belda M, Juruš P, Benešová N, Lopata J, Vlček O, Damašková D, Eben K, Derbek P, Maronga B, Kanani-Sühring F (2017) PALM-USM v1.0: A new urban surface model integrated into the PALM large-eddy simulation model. Geosci Model Dev 10(10):3635–3659, DOI 10.5194/gmd-10-3635-2017

Roupioz L, Kastendeuch P, Nerry F, Colin J, Najjar G, Luhahe R (2018) Description and assessment of the building surface temperature modeling in LASER/F. Energy Buil 173:91–102, DOI 10.1016/j.enbuild.2018.05.033

Rubin M (1985) Optical properties of soda lime silica glasses. Sol Energ Mater 12(4):275–288, DOI 10.1016/0165-1633(85)90052-8

Rupp I, Péniguel C (2014) Syrthes 4.2 user manual. EDF R&D, Tech rep

Stevens B, Moeng CH, Sullivan PP (1999) Large-eddy simulations of radiatively driven convection: Sensitivities to the representation of small scales. J Atmos Sci 56(23):3963 – 3984, DOI 10.1175/1520-0469(1999)056<3963:LESORD>2.0.CO;2

Stewart ID, Oke TR (2012) Local Climate Zones for urban temperature studies. Bull Am Meteorol Soc 93(12):1879 – 1900, DOI 10.1175/BAMS-D-11-00019.1

Stretton MA, Morrison W, Hogan R, Grimmond S (2022) Evaluation of the SPARTACUS-Urban radiation model for vertically resolved shortwave radiation in urban areas. Boundary-Layer Meteorology DOI 10.1007/s10546-022-00706-9

Strømann-Andersen J, Sattrup P (2011) The urban canyon and building energy use: Urban density versus daylight and passive solar gains. Energy Buil 43(8):2011–2020, DOI 10.1016/j.enbuild.2011.04.007

Thomas C, Doz S, Briottet X, Lachérade S (2011) AMARTIS v2: 3D radiative transfer code in the [0.4; 2.5 um] spectral domain dedicated to urban areas. Remote Sens 3(9):1914–1942, DOI 10.3390/rs3091914

UN (2019) World urbanization prospects - the 2018 revision. Department of Economic and Social Affairs, Tech Rep ST/ESA/SER.A/420

Villefranque N, Fournier R, Couvreux F, Blanco S, Cornet C, Eymet V, Forest V, Tregan JM (2019) A path-tracing Monte Carlo library for 3-D radiative transfer in highly resolved cloudy atmospheres. J Adv Model Earth Syst 11(8):2449–2473, DOI 10.1029/2018MS001602

Villefranque N, Hourdin F, d'Alençon L, Blanco S, Boucher O, Caliot C, Coustet C, Dauchet J, Hafi ME, Eymet V, Farges O, Forest V, Fournier R, Gautrais J, Masson V, Piaud B, Schoetter R (2022) The "teapot in a city": A paradigm shift in urban climate modeling. Science Advances 8(27):eabp8934, DOI 10.1126/sciadv.abp8934

Vinet J (2000) Contribution à la modélisation thermo-aéraulique du microclimat urbain. Caractérisation de l'impact de l'eau et de la végétation sur les conditions de confort en espaces extérieurs. Dissertation, Université de Nantes, France

Yang L, Yan H, Lam JC (2014) Thermal comfort and building energy consumption implications – a review. Appl Energy 115:164 – 173, DOI

http://dx.doi.org/10.1016/j.apenergy.2013.10.062